MATERIALS SCIENCE

A soft implantable energy supply system that integrates wireless charging and biodegradable Zn-ion hybrid supercapacitors

Hongwei Sheng[1], Li Jiang[2], Qi Wang[1], Zongwen Zhang[3,4], Yurong Lv[2], Hongyun Ma[1], Huasheng Bi[1], Jiao Yuan[1,5], Mingjiao Shao[1], Fengfeng Li[1], Wenquan Li[5], Erqing Xie[1], Youdi Liu[6], Zhaoqian Xie[3,4], Jing Wang[2]*, Cunjiang Yu[6,7]*, Wei Lan[1]*

The advent of implantable bioelectronic devices offers prospective solutions toward health monitoring and disease diagnosis and treatments. However, advances in power modules have lagged far behind the tissue-integrated sensor nodes and circuit units. Here, we report a soft implantable power system that monolithically integrates wireless energy transmission and storage modules. The energy storage unit comprises biodegradable Zn-ion hybrid supercapacitors that use molybdenum sulfide (MoS_2) nanosheets as cathode, ion-crosslinked alginate gel as electrolyte, and zinc foil as anode, achieving high capacitance (93.5 mF cm^{-2}) and output voltage (1.3 V). Systematic investigations have been conducted to elucidate the charge storage mechanism of the supercapacitor and to assess the biodegradability and biocompatibility of the materials. Furthermore, the wirelessly transmitted energy can not only supply power directly to applications but also charge supercapacitors to ensure a constant, reliable power output. Its power supply capabilities have also been successfully demonstrated for controlled drug delivery.

INTRODUCTION

Advances in high-performance, minimally invasive implantable devices are crucial to achieving long-term, reliable, and safe biosensing and biostimulation (1–6). Although soft, flexible implantable sensors and stimulators evolve rapidly, the development of implantable power modules has been left behind (7). An urgent need exists for developing biocompatible, biodegradable wireless power supply systems, thereby addressing the issues associated with tethered connections and nonrechargeable batteries, including chronic inflammation and secondary surgery for extraction or replacement. Nevertheless, it remains challenging to simultaneously impart power supply modules with excellent energy supply capabilities, tissue-level softness, good biocompatibility, and ideal biodegradability. For instance, energy storage devices (e.g., batteries and supercapacitors) have highlighted different important aspects of implantable applications by using soft (8), biocompatible (9), and biodegradable materials (10–18). Although biodegradable Zn- and Mg-based batteries with easy deployment and high energy density have recently been reported (11, 18), generally these galvanic cells can only be used once, with uncontrolled discharge and inadequate stability. In addition, the power generated is not sufficient to meet the needs in many biomedical applications. Supercapacitors with high-power storage capacity and excellent cyclic stability provide a means to complement or replace batteries. In addition, it can discharge large current in a short time, due to its low energy density, even if short-circuited is also harmless to the human body, which is different from batteries. Yet, this also leads to their inability to provide sustained power to implantable devices over extended durations, which can only be recharged by traditional wired means after being exhausted, while transcutaneous leads have problems associated with sepsis and inconvenience activities. Meanwhile, various complementary powering strategies have been developed to extend their lifetime and even offer independent power supplies. In particular, electromagnetic radiation-based wireless power transmission (19–21) stands out from many other energy-harvesting schemes using biofuel cells (22), nanogenerators (23, 24), or photovoltaic devices (25–27), due to its design flexibility, on-demand supply, and advantages in the amount and stability of the output power. However, adverse biological effects such as overheating from long-term exposure to high power have greatly limited its capability to independently and continuously supply power (28, 29). Hence, now and in the future, we will witness a growing inclination toward the development of integrated hybrid energy-harvesting and storage systems. These innovative systems are capable of harvesting energy from external sources to supply power alone and can be stored, providing a constant stream of energy for electronic devices.

Here, we propose a soft, wireless implantable power system with simultaneously high energy storage performance and favored tissue-interfacing properties. A wireless charging module (receiving coil and rectifier circuit) is integrated with an energy storage module (tandem Zn-ion supercapacitors), which can not only output DC voltage instantly but also supply power sustainably for an extended period of time. This design maximizes the advantages of

[1]School of Physical Science and Technology, Lanzhou University, Lanzhou, Gansu 730000, China. [2]School of Stomatology, Lanzhou University, Lanzhou, Gansu 730000, China. [3]State Key Laboratory of Structural Analysis, Optimization and CAE Software for Industrial Equipment, Department of Engineering Mechanics, Dalian University of Technology, Dalian, Liaoning 116023, China. [4]Department of Engineering Mechanics, Dalian University of Technology, Dalian 116024, China. [5]School of Physics and Electronic Information Engineering, Qinghai Normal University, Xining, Qinghai 810008, China. [6]Department of Engineering Science and Mechanics, Pennsylvania State University, University Park, PA 16802, USA. [7]Department of Biomedical Engineering, Department of Materials Science and Engineering, Materials Research Institute, Pennsylvania State University, University Park, PA 16802, USA.
*Corresponding author. Email: lanw@lzu.edu.cn (W.L.); wangjing@lzu.edu.cn (J.W.); cmy5358@psu.edu (C.Y.)

supercapacitors, with their high power density and long life, effectively compensating for the drawbacks of low energy density and limited continuous power supply capability. With its soft form factor and tissue integrability, the integrated power system can adhere to curved biological surfaces and achieve good biocompatibility both in vitro and in vivo. In particular, the energy storage module is fully made of biodegradable materials while achieving high electrochemical performance (including a high capacitance of 93.5 mF cm^{-2} and a high output voltage of 1.3 V), and its charge storage mechanism is further revealed by comprehensive characterizations. Detailed investigations of the dissolution and biodegradability characteristics of the materials and devices demonstrate their potential for transient, implantable bioelectronic applications, as exemplified by a biodegradable, wirelessly powered drug delivery system (DDS).

RESULTS

Wireless energy transmission and storage device

For implantable bioelectronics, in vivo diagnosis and treatment require large energy reservoirs to ensure stable and reliable operation. However, it remains an unmet challenge to develop integrated power sources for implantable scenarios. First, they demand good biocompatibility and low cytotoxicity with minimal invasiveness for biological systems while ensuring long-time, stable operation of power sources inside the body. Second, tissue-interfaced power sources need to have soft and flexible form factors that can adapt to the curvilinear surfaces of soft tissues and organs. To address the issues, we construct a wireless power system that can wirelessly receive energy from the outside body and store it to power implantable electronic devices (Fig. 1A). The wireless power system consists of three parts: an energy storage unit, a rectifier module, and a magnesium (Mg) receiving coil. Specifically, a soft polymer substrate consisting of poly(L-lactic acid) and poly(trimethylene carbonate) (PLLA-PTMC) is integrated with four biodegradable Zn-MoS$_2$ hybrid supercapacitors in series to serve as an energy storage unit. Although previous studies have demonstrated the construction of high-performance supercapacitors using MoS$_2$/reduced graphene oxide (rGO) heterojunction electrodes and/or alginate gel electrolytes (30, 31), they are nonbiodegradable, contain toxic and harmful substances, and have risks of electrolyte leakage. Thus, they are not suitable for in vivo implantable medical applications. Unlike conventional supercapacitors, to avoid the risks effectively, we need to redesign the electrode materials and electrolyte under the premise of satisfying transient properties and good biocompatibility. To maintain stable device performance in bending conditions, different components are connected by serpentine electrodes, forming an island-bridge structure (fig. S1A). Furthermore, a laser-patterned Mg coil allows the conversion of received electromagnetic waves to a direct current (DC) output via a miniaturized rectifying module. The stacked layers, number of turns, and geometries of Mg coils (fig. S1B) can be tailored to meet specific requirements. For example, in this system, 30 turns of an Mg coil or multilayer coil stack will suffice for induction, whereas more turns require a larger space. The integrated power supply device can not only store energy by supercapacitors but also directly generate stabilized and sustained DC power after rectifying (Fig. 1B). After the wireless charging is turned off, supercapacitors can be used to continue supplying power (fig. S2A). In addition, the

introduction of supercapacitors also helps to mitigate the negative effects of long-term electromagnetic exposure to a certain extent. The rectifying characteristics of the wireless power transfer unit including the Mg coil and rectifier module are shown in fig. S2B. A successful wireless charging process is also confirmed by the continuous discharge of the supercapacitor array at varying current densities (fig. S2C). This process induces no notable heating (fig. S3). Despite the use of a rigid rectifier circuit, it can be readily integrated into the overall soft and deformable system. The serpentine interconnects and the geometric layouts of the functional components are guided by the mechanical theory, ensuring exceptional mechanical performance through the integrated energy supply system. All components are approximately located at the mechanical neutral plane between thin (thickness, 0.2 mm) and soft (modulus, 163 kPa) top/bottom PLLA-PTMC layers to minimize the applied strain/stress during deformation. Figure 1D and fig. S4 show that the simulated equivalent strains in the Mg layers remain lower than the elastic limit (0.3%) in ~30° twisted and ~180° bent devices. For example, the integrated power system can be adaptive to curved surfaces such as biological tissue (Fig. 1C), human skin, and glassware with different curvatures (fig. S5). The device wirelessly charges a 2 × 2 array of tandem supercapacitors to ~5 V within 2 min. After that, it can light up seven light-emitting diodes (LEDs) (fig. S6A). The device sustains a stable power supply under various mechanical deformations (fig. S6B), including bending and crumpling, without varying the light intensity of the powered LED.

To assess the degradation behavior of the integrated power system, accelerated hydrolysis is observed in phosphate-buffered saline (PBS) solutions (pH 7.4, 80°C) at various stages (Fig. 1E and fig. S7). The results showed that the external PLLA-PTMC encapsulation layer disappeared within 3 days, followed by the complete dissolution of the Mg interconnects and the receiving coil after ~15 days, as well as the exposure of the rectifier module and the structural damage to all supercapacitors. To facilitate further observation, the nondegradable rectifier module was removed in the subsequent tests. The next 40 days witnessed the Zn-negative and MoS$_2$/rGO-positive morphological transition from intact electrodes to negligible black spots. In addition, it is of utmost importance to showcase the results and analysis of the encapsulated device's performance and longevity when operated wirelessly in vivo. After wireless charging, the galvanostatic discharge curves at different intervals (1, 3, 5, 7, and 10 days) indicate that the encapsulated device could operate effectively for up to 10 days (fig. S8). It is worth noting that the desired functional lifetime can be enhanced by manipulating factors such as thickness, microstructure, chemistry, and molecular weight of the encapsulating layer. In addition, alternative biodegradable encapsulating materials could also be explored to achieve this goal.

Characterization of MoS$_2$ cathode

Two-dimensional (2D) molybdenum disulfide (MoS$_2$) has been extensively investigated for its unique photoelectric properties, mechanical flexibility, and good biocompatibility/biodegradability (32). As a pseudocapacitive material, MoS$_2$ has a layered/tunneled structure with a covalently bound S-Mo-S sandwich type, which contributes to a high theoretical specific capacitance (1504 F g^{-1}) and excellent intrinsic ionic conduction (33). However, the small interlayer spacing and poor electron transferability still cause a
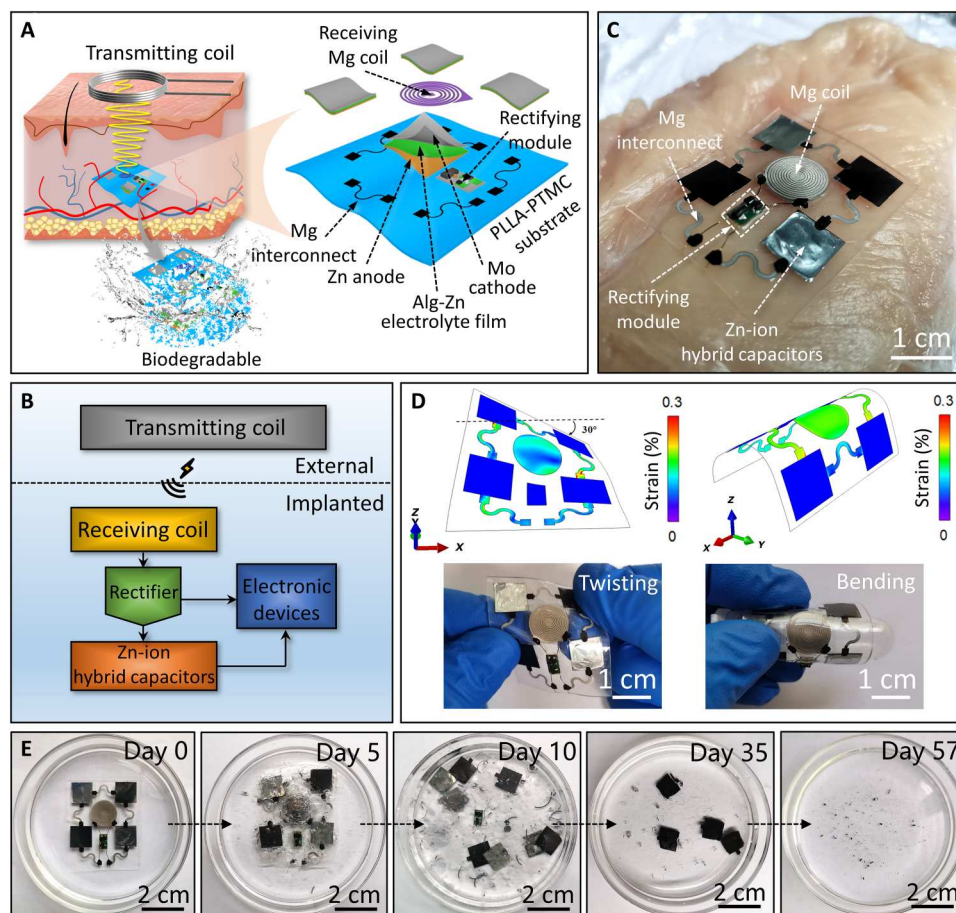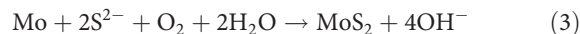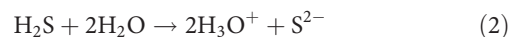
Fig. 1. A wireless energy-harvesting and storage device. (**A**) Illustration showing the exploded schematic view of the device structure. (**B**) Schematic illustration of the integrated power system for powering implantable electronics. (**C**) Photograph of the integrated energy supply system attached to the muscle tissue. (**D**) Result of finite element simulation and photographs of the device in twisted and bent configurations. (**E**) Photographs collected at various stages of the accelerated dissolution of the device in 0.1 M PBS (pH 7.4, 80°C). Photo credit: H. W. Sheng, Lanzhou University.

large gap between the theoretical and actual capacitances, thus limiting the power storage capability of MoS_2-based supercapacitors. To improve the capacitance, oxygen-incorporated MoS_2 was developed with enlarged interlayer spacing (*34*), making it promising for a high energy storage supercapacitor in concomitancy with desired biodegradable properties by MoS_2 (Fig. 2A). The growth of MoS_2 nanosheet arrays involves decomposing thiourea into sulfur ions (S^{2-}) and reacting with outer Mo atoms on a water-soluble Mo foil. During the reaction, metallic Mo becomes MoS_2 nanosheets via the nanoscale Kirkendall effect. Because metal cations have smaller ionic radii than anions, they diffuse faster outward than anions that diffuse inward. As the MoS_2 layer grows, it will inhibit the inward diffusion of outer S^{2-} ions and the outward diffusion of inner Mo cations, which is coupled with the formation of the Mo—O bonds. The possible chemical reactions at the solid-liquid interface can be described as follows (*35*)

$$NH_2CSNH_2 + 2H_2O \rightarrow NH_3 \uparrow + H_2S \uparrow + CO_2 \uparrow \qquad (1)$$

$$H_2S + 2H_2O \rightarrow 2H_3O^+ + S^{2-} \qquad (2)$$

$$Mo + 2S^{2-} + O_2 + 2H_2O \rightarrow MoS_2 + 4OH^- \qquad (3)$$

By a simple and controlled hydrothermal conversion process, MoS_2 is composited with a small amount of rGO to enhance electron transferability (*36*). Eventually, MoS_2/rGO hybrid nanosheets are formed in situ on the Mo foil surface.

MoS_2/rGO hybrid nanosheets were characterized by scanning electron microscopy (SEM) and transmission electron microscopy (TEM). In Fig. 2 (B and C), the MoS_2/rGO composite has a 3D morphology, with vertically aligned MoS_2 nanosheets uniformly grown on the Mo foil surface (fig. S9). The MoS_2/rGO nanosheet arrays are about 200 nm thick, as seen in Fig. 2D. Notably, MoS_2/rGO nanosheets are interconnected with each other to form a highly open structure with a large surface area, which can greatly boost electrochemical performance. Figure 2 (E and F) shows the curled and
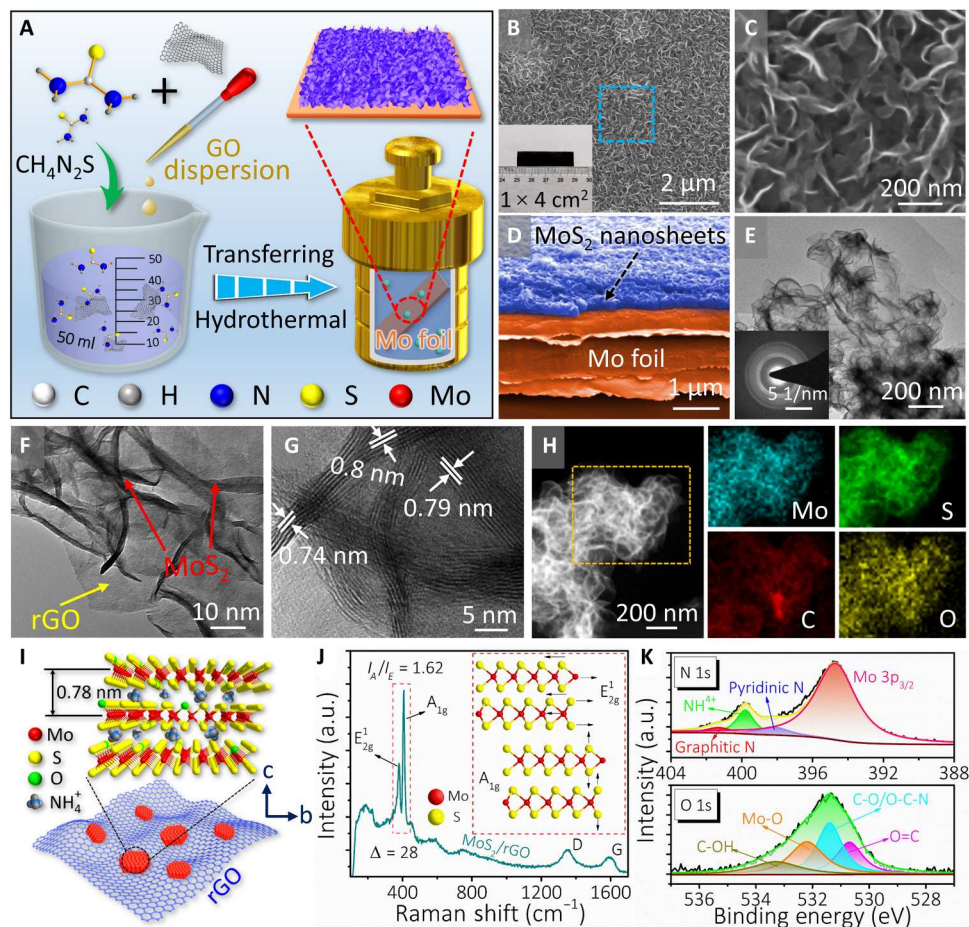
Fig. 2. Preparation and structural characterization of the MoS₂/rGO cathode. (**A**) Schematic diagram of the preparation process of MoS₂/rGO electrode. (**B** and **C**) Top-view and (**D**) cross-sectional SEM image of MoS₂/rGO electrode. Inset in (B) is a photograph of the MoS₂/rGO electrode. (**E** and **F**) TEM and (**G**) high-resolution TEM images of exfoliated MoS₂/rGO nanosheets. Inset in (E) shows the corresponding SAED pattern. (**H**) Acquired EDS elemental mapping of MoS₂/rGO nanosheets. (**I**) Structural models of the O-incorporated and ion-intercalated MoS₂ with enlarged interlayer spacing. (**J**) Raman spectra of MoS₂/rGO electrode. Inset is a schematic of the typical vibration modes for MoS₂. a.u., arbitrary units. (**K**) XPS spectra covering N 1s and O 1s orbitals.

wrinkled MoS₂ nanosheets as supported by rGO. In addition, the selected-area electron diffraction (SAED) pattern (inset of Fig. 2E) suggests that the synthesized MoS₂ nanosheets are polycrystalline. The high-resolution TEM image of the exfoliated MoS₂ nanosheets shown in Fig. 2G displays the interlayer spacing ranging from 0.74 to 0.80 nm, which is larger than the intrinsic d-spacing (~0.62 nm) of MoS₂ (002) lattice plane. Lattice distortion and atomic defects can be observed in fig. S10, as also confirmed by x-ray diffraction (XRD) analysis (fig. S11). We further performed a chemical analysis of MoS₂/rGO nanosheets. Elemental mappings in Fig. 2H confirm the uniform distribution of Mo, S, O, C, and N elements (fig. S12) throughout the MoS₂/rGO nanosheets, which is consistent with the results from energy-dispersive x-ray (EDX) analysis and x-ray photoelectron spectroscopy (XPS) spectrum (fig. S13, A and B). All the above results reveal that it can be the expanded interlayer spacing of MoS₂ nanosheets that potentially contributes to the improved electron/ion transport property (Fig. 2I). In Raman spectra for MoS₂/rGO hybrid (see Fig. 2J), two characteristic peaks at 379 and 407 cm⁻¹ correspond to the in-plane E1 2g and the out-of-plane A₁g vibration modes of

thermodynamically stable 2H-MoS₂, respectively. Meanwhile, the frequency difference (Δk) between E1 2g and A₁g modes is 28 cm⁻¹, revealing a few-layer and small-size feature of the as-prepared MoS₂ nanosheets (*37*). Two additional peaks can stem from the D-band (a breathing mode of symmetry A₁g) around 1354 cm⁻¹, and the G-band (E₂g symmetry) at 1597 cm⁻¹, suggesting the successful reduction of GO to rGO (fig. S14) (*38*, *39*).

High-resolution XPS spectroscopy was further applied to investigate the chemical states of Mo, S, N, O, and C elements for the composite electrode. In addition to a weak peak at 226.0 eV of S 2s orbital, the core-level spectrum of Mo 3d spectrum can be deconvoluted into four appropriate peaks, as shown in fig. S13C. Two main peaks at 232.0 and 228.8 eV correspond to Mo 3d₃/₂ and Mo 3d₅/₂ spin-orbit peaks of the Mo⁴⁺ oxidation state, respectively, indicative of the presence of the dominant 2H phase of MoS₂ (*40*). In addition, the other two minor peaks at 233.0 and 229.5 eV reveal the existence of a smaller 1T phase of MoS₂ (*41*). In the S 2p region of the spectrum (fig. S13D), two major peaks at 161.6 and 162.7 eV can be assigned to the S 2p₃/₂ and S 2p₁/₂ binding energies for S²⁻ in MoS₂, respectively. In addition, the peak at 163.5 eV can originate

from a small number of vacancies in MoS_2 (42). MoS_2 with S defects can lead to more active ionic adsorption sites per volume (fig. S13E). The enlarged interlayer spacing can mainly be attributed to the oxygen incorporation and the intercalation of hydrated ammonium ions (NH_4^+) inside the lattice of MoS_2 nanosheets in the hydrothermal sulfidation process. This is confirmed by the presence of a distinct N 1s peak around 400.0 eV, albeit the partial overlap of N 1s and Mo 3p spectra (Fig. 2K, top) (43). The other two relatively weak peaks at 398.2 and 401.3 eV correspond to the main pyridinic N and smaller graphic N in the rGO, respectively (44). In addition, the N doping and the reduction of GO to rGO are verified by the C 1s XPS spectrum (fig. S13F) at a binding energy of 284.6 (C—C/C=C), 285.2 (C—N), and 286.4 eV (C—O). Four peaks for O 1s spectrum (Fig. 2K, bottom) can be ascribed to C—OH (533.3 eV), Mo—O (532.2 eV), C—O/O—C—N (531.4 eV), and O=C (530.7 eV) bonds, respectively (40). Furthermore, the presence of Mo—O bonds confirms the successful oxygen incorporation rather than the surface oxidation in the MoS_2 structure. According to previous studies, oxygen incorporation could effectively regulate the electronic structure of MoS_2 (45), resulting in enhanced intrinsic conductivity. Together, we expect that the combination of rGO and oxygen-incorporated MoS_2 nanosheets can yield enhanced electrochemical properties.

Design of electrolyte film

Electrolytes also play a crucial role in energy storage device performance. For implantable energy storage devices, to effectively improve leakage issues, internal short-circuiting, and ease of packaging, quasi–solid-state hydrogels composed of organic polymer matrices with ion-conducting species are often used as electrolytes. In general, the following characteristics are desired for hydrogel electrolytes, including high ionic conductivity, high electrochemical stability, and excellent flexibility (46). Good biocompatibility and biodegradability are also key characteristics to be considered for biodegradable implantable applications. Therefore, we selected typical sodium alginate (Alg-Na), a low-cost and easily processed biopolymer extracted from nature, as the polymer matrix immobilized with liquid electrolytes. On the basis of the interaction between Alg-Na and the active Zn^{2+}, a quasi–solid-state gel electrolyte film was prepared through a direct ion cross-linking method (Fig. 3A). As shown in Fig. 3B, an Alg-Zn electrolyte film is highly transparent and mechanically robust, and flexible (fig. S15), which can withstand a weight of as high as 100 g while twisting. The SEM images of the Alg-Zn electrolyte film (fig. S17B) reveal its porous, wrinkled surface. The cross-linking chains can be hypothesized to be arranged layer by layer (fig. S16), consistent with the cross-sectional morphology (Fig. 3C) of the Alg-Zn gel electrolyte film. The corresponding energy-dispersive spectroscopy (EDS) element mappings (fig. S17C) indicate the homogeneous distribution of Zn, Cl, and O components. The successful cross-linking of Alg-Zn gel is confirmed by Fourier transform infrared spectroscopy (FTIR), as shown in fig. S18A. The clear broadband centered at 3394.0 cm^{-1} is assigned to the hydrogen-bonded O—H stretching vibrations, and the weak signal at 2970.1 cm^{-1} is due to C—H stretching vibrations on the alginate chains. The band at about 1626.8 and 1435.8 cm^{-1} can be ascribed to the asymmetric stretching and symmetric stretching of the carboxylate O—C—O vibrations on the alginate polymer chains, respectively. Compared to the Alg-Na before and after cross-linking, the asymmetric stretching vibration peak of O—C—O

groups for Alg-Zn shifts to higher values, which can result from the formation of coordination bonds between carboxylate groups and Zn^{2+} (47). With Zn^{2+} ions replacing Na^+ ions, a new chemical environment has been created around the carbonylate groups; the charge density and the radius of the cation have also changed (48). The weak band at 1435.8 and 1301.5 cm^{-1} may be caused by the C—OH deformation vibration of the carboxylate group and the C—C—H deformation vibration of pyranose rings, respectively (49). The thermogravimetric analysis (TGA) indicates the good thermal stability of the Alg-Zn electrolyte below 150°C (fig. S18B).

To investigate the reversibility and stability of the device, the metallic Zn anode was tested in the Alg-Zn electrolyte film in comparison with that in 1 M $ZnCl_2$ using a Zn//Zn symmetric cell under galvanostatic conditions. The use of Alg-Zn electrolyte enables the Zn anode to show much superior electrochemical stability. In this case, after more than 600 hours of plating/stripping with a current density of 1.13 mA cm^{-2} (>1000 cycles) for 30 min for each cycle (Fig. 3D), the Zn//Zn symmetric cell shows a consistently low voltage polarization without any short circuit or overpotential rising issues. The Zn plated on the substrates still shows a relatively dense and dendrite-free morphology after cycling (fig. S19A), suggesting a stable and homogeneous Zn plating/stripping process. By contrast, a sudden polarization and short circuit occur after only about 60 hours of plating/stripping in a 1 M $ZnCl_2$ solution, which suggests severe corrosion of metallic Zn and penetration of membrane by zinc dendrites. After cycling in the liquid electrolyte, the surface of Zn foil is covered with micro-sized plates with sharp edges (fig. S19B), indicating an inhomogeneous Zn plating/stripping process that can largely limit the life span of the Zn anode. The Zn deposition process in both cases is illustrated in fig. S13 (C and D). In a liquid electrolyte, the Zn deposition process is consistently interfered with by side reactions, including Zn corrosion and the parasitic hydrogen evolution reaction due to the existence of detrimental water molecules. According to the reported tip-growth theory, Zn tips are unavoidably growing into large Zn flakes with bulk accumulation and uneven deposition in the electrolyte, thereby eventually forming cracks and "dead" Zn without electrochemical activity. On the contrary, the migration of the Zn^{2+} ions in the Alg-Zn electrolyte film is confined by the carboxylate groups while interacting with each other, which can guide their migration and serve as curb chains that firmly bind the Zn^{2+} ions. As a result, large Zn plate aggregations around the free tips can be greatly inhibited and even terminated, leading to uniform and dendrite-free Zn plating. The alternating-current (AC) impedance spectra of a 125-µm-thick Alg-Zn electrolyte film are shown in Fig. 3E. The corresponding ionic conductivity (σ) was calculated by σ = $L/(AR)$, where R, A, and L are the ohmic resistance (in ohms), thickness (in centimeters), and area (in square centimeters), respectively. It should be noted that the Alg-Zn electrolyte film exhibits a high ionic conductivity of 1.65 × 10^{-2} S cm^{-1}, compared with other reported gel electrolytes (50–52). Besides, the Zn^{2+} transference number of Alg-Zn electrolyte film at ambient temperature is tested using a Zn/Alg-Zn/Zn symmetric cell with a constant polarization potential of 10 mV (Fig. 3F). The Zn^{2+} transference number was calculated on the basis of the classical formula (53)

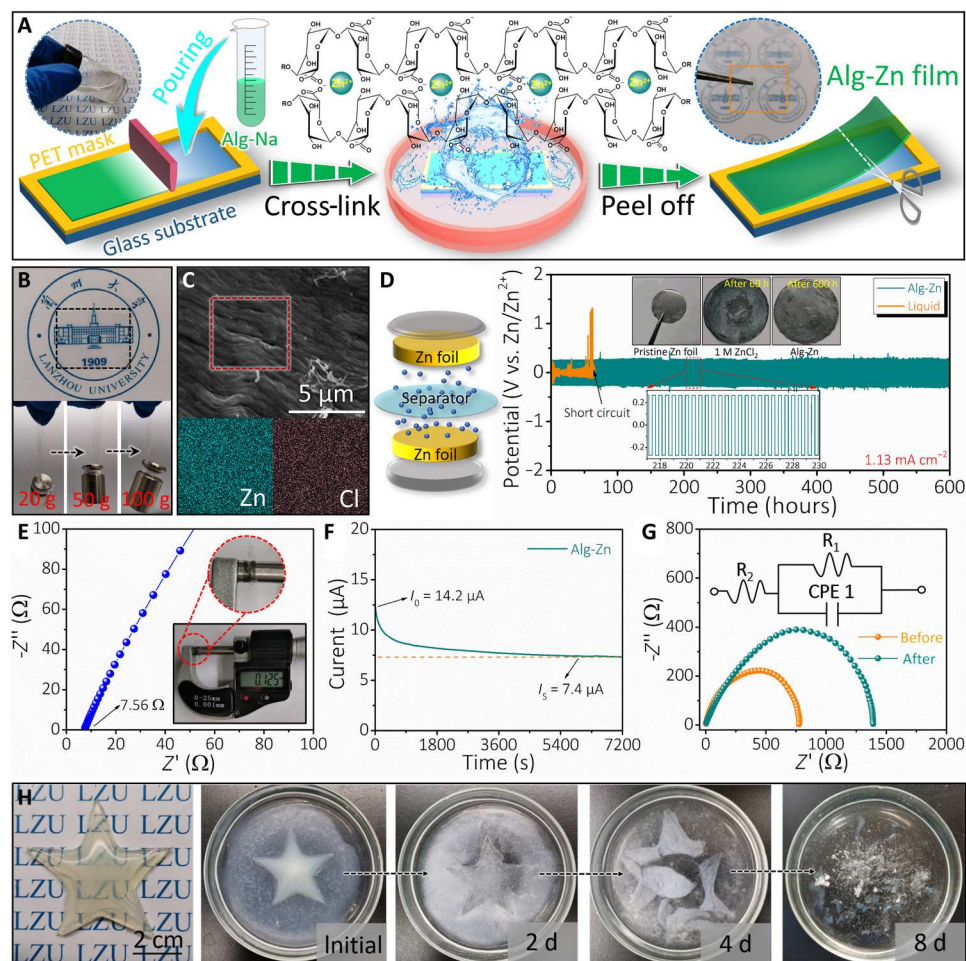$$T_+ = \frac{I_s(\Delta V - I_0 R_1^0)}{I_0(\Delta V - I_s R_1^s)} \qquad (4)$$

Fig. 3. Design of the Alg-Zn electrolyte film. (**A**) Schematic illustration of the preparation process for Alg-Zn electrolyte film. (**B**) Photograph of the optical transparency and mechanical property of Alg-Zn film. (**C**) Cross-sectional SEM image and the corresponding EDS elemental mapping of Alg-Zn. (**D**) Exploded schematic of Zn//Zn symmetric cell and galvanostatic Zn plating/stripping performance under a current density of 1.13 mA cm^{-2} at room temperature. The insets (top) are the corresponding optical images of the Zn foils after cycled in Alg-Zn and liquid ones. The inset (bottom) is the typical voltage-time profile. Each cycle lasts for 30 min. (**E**) AC impedance spectra of the Alg-Zn electrolyte. Inset is the thickness of the Alg-Zn electrolyte. (**F**) The I-t curve at an applied voltage of 10 mV. (**G**) EIS spectra before and after polarization; inset shows the corresponding equivalent circuit. (**H**) Photographs at various degradation stages in 0.1 M PBS (pH 7.4, 37°C) of the pentagram-shaped Alg-Zn electrolyte film. Photo credit: H. W. Sheng, Lanzhou University.

where I_0 and I_s refer to the initial and steady-state currents, respectively, and ΔV is the potential applied across the cell. R_1^0 and R_1^s are the initial and steady-state resistances of the cell, respectively, determined by impedance spectroscopy (Fig. 3G). From the calculation, the T_+ of Zn^{2+} is 0.51, suggesting a fast ion diffusion kinetics. In addition, using custom-built molds (fig. S17, D and E), this Alg-Zn gel electrolyte was molded into a transparent pentagram-shaped lump (~2 mm thick) to validate its biodegradability in PBS at 37°C (Fig. 3H). After 8 days, the Alg-Zn electrolyte film is fully degraded due to the water-soluble nature of alginate.

The performance of Zn-MoS$_2$ hybrid supercapacitor
On the basis of MoS$_2$/rGO electrode and Alg-Zn electrolyte, a flexible Zn-MoS$_2$ hybrid capacitor was constructed, as depicted in Fig. 4A. Systematic bending tests were conducted to evaluate their mechanical flexibility. Three essential parameters have been widely used to describe their bending status (54): (i) θ, the bending angle;

(ii) R, the curvature radius; and (iii) L, the device length. When L and R were fixed to be 4 and 1 cm, respectively, θ is varied from 30° to 150°, resulting in different stress areas. We constructed a pure bending theoretical model of a Zn-ion hybrid supercapacitor, as illustrated in Fig. 4B. The finite element results (Fig. 4C) of the maximum absolute value of strain ε$_{abs}$ for each material layer at different bending radii are consistent with the theoretical values (55). The capacitance retention (fig. S20) maintains above 85.8% even at a high bending angle of 150° after 100 bending cycles, showing excellent mechanical flexibility and durability. Figure 4D shows the almost quasi-rectangular cyclic voltammetry (CV) curves scanned at various rates of 10 to 100 mV s^{-1}. CV shapes are well maintained in the range of 0.2 to 1.3 V even at the scan rate up to 200 mV s^{-1}, exhibiting a favorable capacitive performance. This was further verified by the triangular-like galvanostatic discharge/charge (GCD) profiles recorded at different current densities of 0.2 to 3 mA cm^{-2} (fig. S22A). A similar electrochemical feature (fig. S21) was
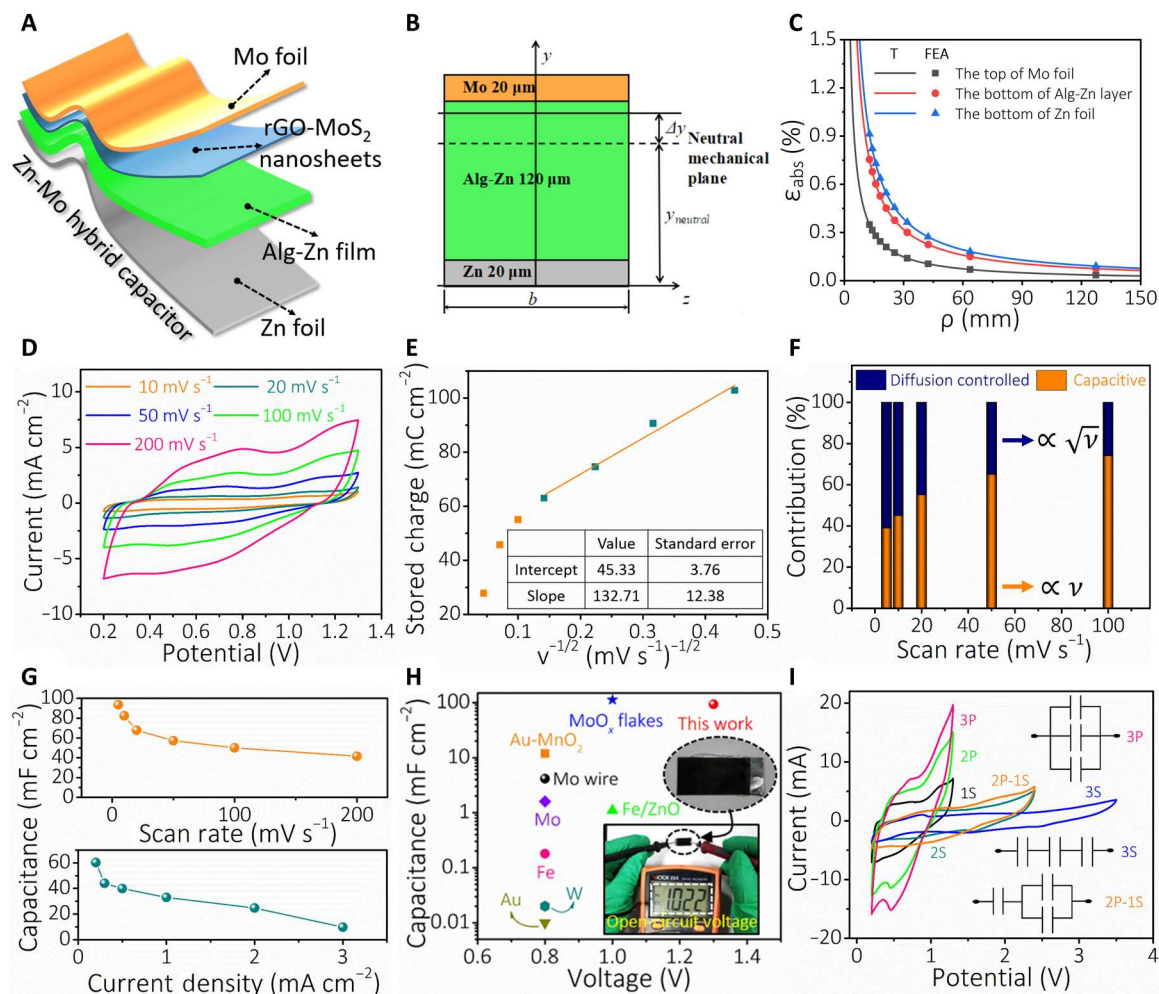
Fig. 4. Performances of Zn-MoS₂ hybrid supercapacitor. (**A**) Schematic illustration for the flexible Zn-MoS₂ hybrid supercapacitor based on the Alg-Zn electrolyte film. (**B**) Schematic diagram of the cross section of Zn-ion hybrid supercapacitor, with the location of the neutral mechanical plane marked by dotted line. (**C**) Theoretical (T) and FEA results of maximum absolute value of strain ε_{abs} in each material layer. (**D**) CV profiles scanned at various rates of 10 to 200 mV s^{-1}. (**E**) Stored charge (C) versus $v^{-1/2}$ for Zn-MoS₂ hybrid supercapacitor. The intercept value represents the surface charge. (**F**) Capacitance contribution of the capacitive and diffusion-controlled process at different scan rates. (**G**) Scan rate–dependent capacitance from galvanostatic discharge/charge measurements. (**H**) Areal capacitance of this work in comparison to that of other reported degradable supercapacitors. The inset is the V_{oc} of an as-prepared Zn-MoS₂ hybrid supercapacitor without charging tested by a multimeter. Detailed values are presented in table S1. (**I**) CV profiles (at 0.1 V s^{-1}) of different devices connected in series and/or parallel. Photo credit: H. W. Sheng, Lanzhou University.

also observed in liquid electrolytes (1 M ZnCl₂). To analyze the electrochemical kinetic processes of the Zn-MoS₂ hybrid supercapacitor, both the Trasatti method (*56*) and k_1, k_2 analyses (*57*) were adopted to distinguish between capacitive and diffusion-controlled contributions. From the former method based on voltammetric charge, the surface-dominant and total charges were estimated to be 45.3 mC cm^{-2} from a C versus $v^{-1/2}$ plot (Fig. 4E) and 128.2 mC cm^{-2} from a $1/C$ versus $v^{1/2}$ plot (fig. S22B), respectively. The latter method was further used to quantify the capacitive and diffusion-controlled current contributions at various scan rates (Fig. 4F and fig. S23). It can be found that nearly 65% of the total current (at 50 mV s^{-1}) is capacitive-limited. As the scan rate increases, the fast capacitive process plays a leading role in total capacitance. In addition, the areal capacitances derived from CV and GCD profiles are plotted as a function of charge/discharge rates in Fig. 4G. The acquired capacitance values using the two approaches are comparable,

reaching the highest capacitance of 93.5 mF cm^{-2}. As shown in Fig. 4H, this asymmetrical electrochemical behavior generates a high open-circuit voltage (V_{oc}) of 1.022 V at both electrodes without charging. In addition, our device achieves a high capacitance and a high output voltage (1.3 V) simultaneously, compared to the existing biodegradable supercapacitors (*10*, *12–14*, *17*, *58–61*) and other supercapacitors using similar materials (table S1) (*62*, *63*). The calculated energy density of a typical Zn-MoS₂ hybrid supercapacitor reaches as high as 1.65 µWh cm^{-2} at a power density of 1.97 mW cm^{-2}. The typical Zn-MoS₂ hybrid supercapacitor also shows excellent cycling stability, retaining 94.6% of the initial capacitance after 800 cycles of charging and discharging (fig. S24). Moreover, these developed Zn-MoS₂ hybrid supercapacitors can be readily connected in series and/or parallel, forming tandem devices to satisfy specific energy/power demands (Fig. 4I). For instance, two tandem devices can successfully power a red LED light

(threshold voltage: ~1.8 V) and an electronic thermometer (fig. S25), demonstrating practical applications for the quasi–solid-state Zn-MoS$_2$ hybrid supercapacitor.

Energy storage mechanism

We performed a comprehensive study on the charge storage mechanism of MoS$_2$ cathodes. The detailed configuration of a Raman cell we used is illustrated in Fig. 5A. Figure 5B shows the ex situ Raman spectra at different discharge/charge stages (marked points: A → I) of the MoS$_2$ cathode for the second cycle. Upon continuous discharging (A → E), the A$_{1g}$ characteristic peak at 407 cm^{-1} becomes broader and the relative intensity ratio of A$_{1g}$/E1 2g decreases from 1.53 to 1.22, suggesting the insertion of Zn^{2+} into the layers of MoS$_2$. When charging back to 1.3 V (E → I), the A$_{1g}$ characteristic peak intensity gradually enhances, and the relative intensity ratio of A$_{1g}$/E1 2g increases from 1.22 to 1.52, which is associated with the extraction of Zn^{2+} from MoS$_2$. The Zn^{2+} intercalation/de-intercalation behaviors were further revealed by TEM (Fig. 5C). After discharging, the interlayer spacing of MoS$_2$ nanosheets increases from 7.4 to 9.8 Å, further confirming the successful intercalation of Zn^{2+} into the host lattice. This result also agrees with the SEM results (fig. S26), where the MoS$_2$ nanosheets in the fully discharged state are slightly thicker than the pristine sample. Figure 5D compares the core-level Mo 3d XPS spectra of the MoS$_2$ cathode under insertion (discharge to 0.2 V) and extraction (charge to 1.3 V) states. At 0.2 V, an increase in the Mo-O peak intensity can be observed, showing its deep discharging nature. On the contrary, when charged to 1.3 V, the Mo-O peak fades away (64). Figure 5E shows the Zn 2p XPS region of fully discharged (0.2 V) and fully charged (1.3 V) electrodes in the second cycle. The intensity of Zn 2p$_{3/2}$ (1021.9 eV) and Zn 2p$_{1/2}$ (1045.2 eV) at the charged state is far below that at the discharged state, which further confirms the insertion/extraction of Zn^{2+} into/from the MoS$_2$ crystals. On the basis of the above results, the chemical mechanism of the Zn-MoS$_2$ hybrid supercapacitor is proposed in Fig. 5G and fig. S27A, and the possible electrochemical reactions between the MoS$_2$ cathode and Zn anode can be summarized as follows
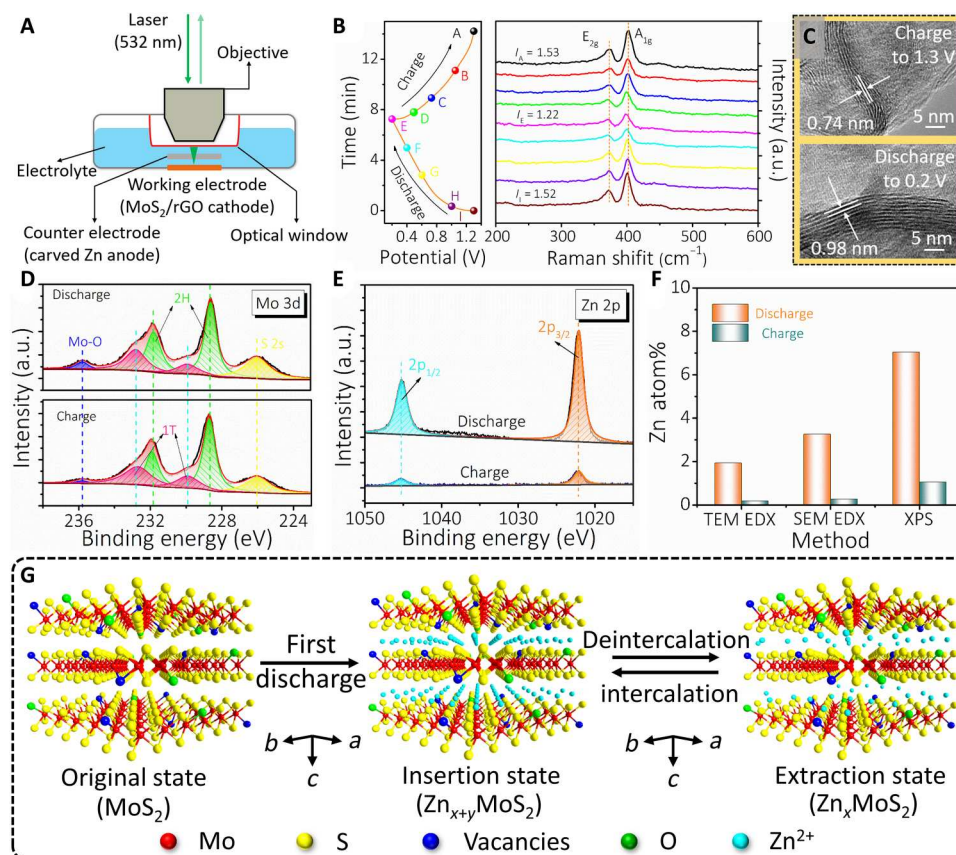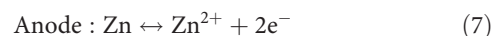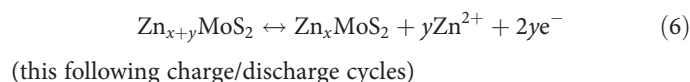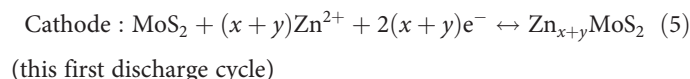
$$\text{Cathode}: MoS_2 + (x+y)Zn^{2+} + 2(x+y)e^- \leftrightarrow Zn_{x+y}MoS_2 \quad (5)$$

(this first discharge cycle)

$$Zn_{x+y}MoS_2 \leftrightarrow Zn_xMoS_2 + yZn^{2+} + 2ye^- \quad (6)$$

(this following charge/discharge cycles)

$$\text{Anode}: Zn \leftrightarrow Zn^{2+} + 2e^- \quad (7)$$

Fig. 5. The energy storage mechanism of MoS$_2$/rGO cathodes. (**A**) Schematic diagram of the setup and (**B**) Raman spectra at different charge/discharge depths (A → I) and the corresponding charge/discharge profiles of the second cycle (at 0.2 mA cm^{-2}) in 1 M ZnCl$_2$ for MoS$_2$/rGO cathode. (**C**) Ex situ TEM images of MoS$_2$ nanosheets in insertion (discharge to 0.2 V) and extraction (charge to 1.3 V) states. The core-level (**D**) Mo 3d and (**E**) Zn 2p XPS spectra of MoS$_2$/rGO cathode in the discharge and charge state. (**F**) The corresponding element atomic % obtained by three different methods, including TEM-EDX, SEM-EDX, and XPS. (**G**) Schematic illustration of the Zn^{2+} intercalation/de-intercalation mechanism for Zn-MoS$_2$ hybrid supercapacitors.

The Zn atomic % of the insertion state (0.2 V) and extraction state (1.3 V) are further revealed by the EDX spectra obtained by three different approaches (Fig. 5F and fig. S27B). In all of these studies, Zn atomic % in the insertion state in MoS_2 nanosheets is significantly higher than in the extraction state, indicating that Zn^{2+} ions can be intercalated/deintercalated almost reversibly.

Biodegradation and cytotoxicity evaluation

Biocompatibility is an important factor in implantable devices involving both device materials and dissociated/leaching products. Figure 6 (A and B) demonstrates the optical images at various stages of the dissolution process of the Zn-MoS_2 hybrid supercapacitor (~200 μm thick) in PBS. Initially, the edges and exterior of a quasi−solid-state, sandwiched Zn-MoS_2 hybrid supercapacitor were encapsulated with poly(lactide-co-glycolide) (PLGA) and wax and then soaked in PBS (pH 7.4, 37°C). After 10 days, the device remains intact (fig. S28, A and B), achieving a stable operation of the device for up to a week (fig. S28, B and C), which is mainly due to the good

water resistance of the wax. To assess the dissolution behavior, accelerated hydrolysis was performed in PBS (pH 7.4) at an elevated temperature (85°C). After 3 days (fig. S29A), the original layer-by-layer structure has been destroyed having two electrodes separated, which indicates the complete degradation of the Alg-Zn electrolyte film. Over the next 15 days, the Zn foil and MoS_2 nanosheets gradually degraded, accompanied by surface cracking and fragmentation of the Mo foil (fig. S29, B and C). Residual Mo needs another 20 days to dissolve into a small amount of oxidized black powder. The active mass loading of our MoS_2/rGO heterojunction electrode is very small, about 0.25 mg cm^{-2}, and mainly MoS_2 nanosheets. The material degradation process involves hydrolysis reactions: e.g., $Zn + 2H_2O \rightarrow Zn(OH)_2 + H_2$; $2Mo + 2H_2O + 3O_2 \rightarrow 2H_2MoO_4$; $2MoS_2 + 7O_2 \rightarrow 2MoO_3 + 4SO_2$; $MoO_3 + 2OH^- \rightarrow MoO_4^{2-} + H_2O$ (65). The dissolution rate of MoS_2 is highly affected by the lattice mismatch, defect, and dislocation regions such as S vacancies and Mo dangling bonds (32). For instance, the defect-free areas have a high kinetic energy barrier, and their chemical
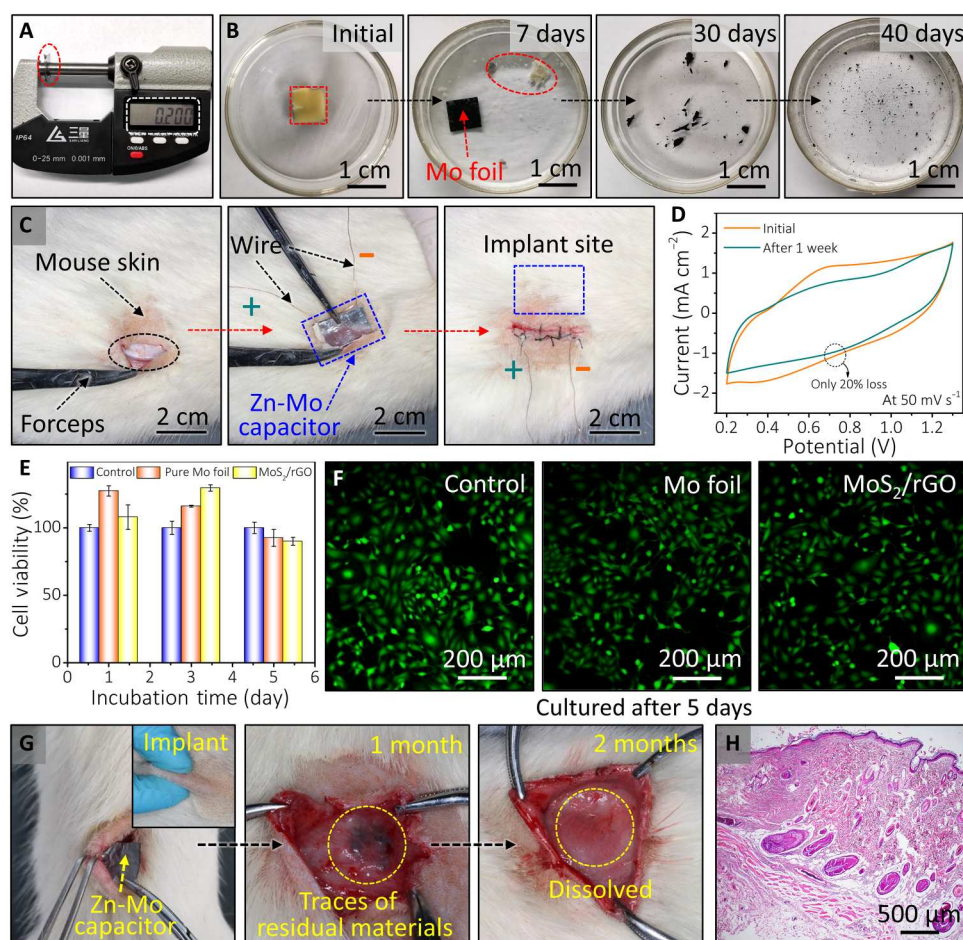

Fig. 6. In vitro and in vivo long-term biocompatibility and degradation evaluation. (**A**) Photographs of thickness for Alg-Zn electrolyte film, measured by an electronic helical micrometer. (**B**) Optical images at various stages of the dissolution for Zn-MoS_2 hybrid supercapacitor immersed in 0.1 M PBS (pH 7.4, 85°C). (**C**) Photographs of the process for an encapsulated Zn-MoS_2 hybrid supercapacitor implanted into the subcutaneous area of an SD rat. (**D**) Comparison of CV curves of an implanted Zn-MoS_2 hybrid supercapacitor after 1 week. (**E**) Cell viability of pure Mo foil and MoS_2/rGO cathode over 1, 2, and 5 days calculated as the fraction of total living cells. (**F**) Fluorescent images displaying the cell viability, with green (calcein-AM)/red (PI) referring to live/dead cells, respectively. (**G**) In vivo degradation test of Zn-MoS_2 hybrid supercapacitor implanted in the subcutaneous area of SD rats: (left) implantation, (middle) 1 month after implantation, and (right) 2 months after implantation, suggesting the complete dissolution of the device. (**H**) H&E staining of excised tissue from the implanted site after 2 months. Photo credit: H. W. Sheng, Lanzhou University.

stability is relatively high at ambient conditions. Unlike the chemical vapor deposition (CVD)-grown MoS_2 crystals previously reported, our prepared MoS_2 nanosheets have large layer spacing and contain many defects, resulting in a low kinetic energy barrier, which can accelerate the degradation. In addition, previous studies have shown that an appropriate amount of rGO nanosheets can be degraded and excreted through the kidneys (66), showing promising applicability in drug delivery, tissue engineering, diagnostics, and various other biomedical fields. In addition, it has been validated as electrode material alone in biodegradable energy storage devices (67). On the other hand, the dissolution rates of Zn and Mo foils are reported to be ~3.5 and 0.02 μm day^{-1} in simulated biofluids (pH 7.4, 37°C), respectively. The degradation rates of the Zn-Mo supercapacitor materials (e.g., metallic foils, active materials, and Alg-Zn) are comparable with the reported results in the literature (68). It is noted that Zn and Mo are essential trace elements to the growth and development of the human body. At the same time, the doses of the dissolved Zn and Mo from our device are far below their daily intakes and can therefore be considered biosafety for implantable and degradable utilities (69, 70). Moreover, MoS_2/rGO nanosheets exhibit low cytotoxicity and thus high in vitro biocompatibility as manifested by the proliferation of the coincubated NIH/3T3 cells in 1, 2, and 5 days (figs. S30 to S32). The decent biocompatibility of other components (Zn and electrolyte film) has been well demonstrated in previous works (71), validating the overall biocompatibility of our device.

To evaluate the in vivo device performance, the PLGA-encapsulated Zn-MoS_2 hybrid supercapacitors were implanted into the dorsal subcutaneous area of Sprague-Dawley (SD) rats (Fig. 6C). After 1 week (Fig. 6D), the areal capacitance of a supercapacitor has only degraded by 20% as examined by the CV profile. The decreased capacitance might be attributed to the infiltration of body fluid of SD rats, the corrosion of electrodes, and the solvation of hydrogel electrolyte. It is worth noting that the degradation rate can be rationally tailored through appropriate packaging strategies. In addition, the Cell Count Kit-8 (CCK-8) assay and calcein-AM/propidium iodide (PI) staining were conducted to investigate the cytotoxicity of MoS_2/rGO cathode and pure Mo foil current collector. Here, NIH/3T3 cells, mouse embryonic fibroblast cells, were selected and directly cultured on their surfaces. After coincubation of NIH/3T3 cells with different materials for different times (1, 2, and 5 days), the corresponding cell viability, fluorescent images, and micromorphology of the cells are shown in Fig. 6 (E and F) and figs. S30 to S32, respectively. It can be observed that the cellular density of NIH/3T3 cells increases with incubation time. Some cell clusters formed and even grew into a confluent cell monolayer after a 5-day incubation. Moreover, the existence of trace amounts of Mo compounds also accelerates the growth of the NIH/3T3 cells, coinciding with the results reported previously (14). Both the relative cell viability and fluorescent images indicate that the MoS_2/rGO cathodes have low cytotoxicity to the NIH/3T3 cells. Without encapsulation, the Zn-MoS_2 hybrid supercapacitors degrade gradually inside the body that leaves traces of residues after 1 month while undergoing complete dissolution within 2 months (Fig. 6G). We further verified the good in vivo biocompatibility of the device at various stages and its products after dissolving, which show minimally adverse reactions to hypodermal (Fig. 6H) and other main organ tissues (figs. S33 and S34). The in vivo degradation differs from that of the in vitro process, probably due to the difference in the aqueous environments and circulation conditions.

Integrated power system for controlled drug release

Implantable DDSs play a vital role in localized, on-demand drug delivery and therapy. By using material screening and structural design, these systems can effectively cater to drug delivery requirements in various pathological environments such as subcutaneous, muscular, vascular, and even the brain (72). To date, most drug delivery devices are nonbiodegradable and designed with a destructive drug release mechanism, which makes them incapable of releasing drugs multiple times or maintaining controlled dosage over time, while necessitating secondary surgery for device extraction after implantable uses (73, 74). Recently, some novel electrically controlled DDSs made of biodegradable materials have been developed (75, 76), addressing drug leakage concerns during implantation and enabling pulsed drug release. Despite this, achieving precise drug release control (including time and rate) remains a great challenge. We developed a compact, biodegradable, and electric field–driven drug delivery device that is wirelessly powered by the power system to achieve programmable, on-demand drug release in vitro. Here, the drug release rate of our device can be controlled by altering the charging depth and times of the energy storage unit. Alternatively, the rectified DC output can directly drive a drug release process. Figure 7A illustrates the drug delivery device composed of biodegradable components, including screen-printed carbon (top and bottom) electrodes, a hot-pressed polylactic acid (PLA) drug reservoir, and a mixed cellulose ester (MCE) membrane. The shape and volume of the reservoir (fig. S35) can be adjusted as required with the top pinhole that is then sealed by an MCE membrane (fig. S36). The detailed fabrication processes of the drug delivery device are shown in fig. S37, with its small size favorable for implantable applications. After the external encapsulation by wax (fig. S38), the size and weight of a single drug delivery device are around 8 mm × 8 mm × 4 mm and 0.3 g, respectively. The drug delivery device also exhibits biodegradability that can be dissolved in a bath of PBS (pH 7.4) at 85°C for 8 days in an accelerated process (fig. S39). For drug release, an electric field is applied between the top and bottom electrodes to drive the movement of the charged drug molecules (Fig. 7B). Even without applying any voltage, the device releases very few ionic drugs by diffusion from the drug-containing hydrogel. Once a DC voltage is applied, ionic drugs are accelerated to migrate to the surrounding fluid through the separation membrane (77). This is consistent with the electrophoretic devices we developed that can effectively and controllably deliver both cationic and anionic drugs. For an exemplified cationic drug [methylene blue (MB)], the leakage of it into PBS solution is quite slow (78), with a very low diffusion coefficient of about 1.36×10^{-7} cm^2/s (fig. S40). Under a positive voltage, MB molecules migrate rapidly across the porous separation membrane to the surrounding fluid (Fig. 7C). The cumulative amount of MB was monitored by optical spectroscopic measurements (Fig. 7D) with an absorption peak at 665 nm, which shows a linear proportional relationship (Fig. 7E). On the other hand, similar to the problem of pure membrane diffusion without electrical stimulation, the drug release dosage was found to be linearly correlated with stimulation duration and voltage amplitude (Fig. 7F and fig. S41), indicating the mass transfer resistance dominated by molecular permeation through a membrane. In another case, we demonstrated the feasibility of
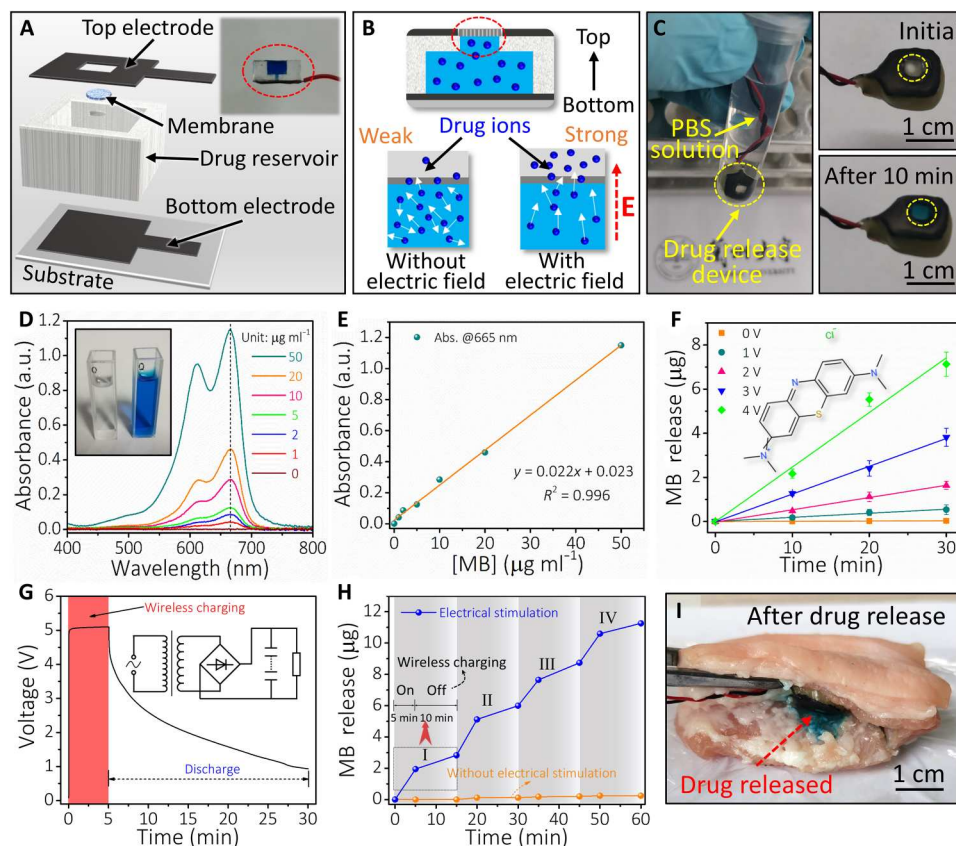
Fig. 7. In vitro drug release demonstration. (**A**) Exploded schematic view of the biodegradable drug release device to show its design. Inset: Side view of the internal drug reservoir filled with the model drug. (**B**) Schematic illustrations of the drug release mechanism from the device. (**C**) Photographs of the encapsulated device submerged in PBS solution: devices with an applied voltage of 4 V for 10 min (right). The separation membrane stained with MB can be observed, suggesting a much faster drug release rate. (**D**) UV-vis spectra of MB at different concentrations in 0.1 M PBS (pH 7.4). (**E**) Beer-Lambert plot of data in (D). (**F**) Cumulative amount of MB released into the surrounding solution at different applied voltages. The error bars indicate the SDs. (**G**) Discharge time of the integrated power system applied to the drug release device after charging. The inset is a simplified circuit diagram. (**H**) Cumulative release of MB from the device after synergistic electrical stimulation of the integrated power system. The arrow above the dotted box indicates the on and off of wireless charging. The "on" state is defined as the utilization of wireless charging to provide energy while simultaneously charging the supercapacitor. Conversely, the "off" state means that the wireless charging is closed and relies entirely on the electrical energy stored in the supercapacitors for drug release. (**I**) Photographs of the drug release device placed between the porcine skin and the muscle tissue after the release of the model drug. MB was selected as a model drug for better visualization of the drug release. Photo credit: H. W. Sheng, Lanzhou University.

releasing an anionic model drug ibuprofen (IBU), which is widely used for anti-inflammation (fig. S42). The release rates under voltage are approximately the same order of magnitude as in a previous study (*77*). In contrast, pure membrane diffusion becomes negligible if no voltage is applied.

Eventually, to demonstrate the figure of merit of our design, the monolithically integrated power system was connected to the drug delivery module. Four tandem Zn-MoS$_2$ hybrid supercapacitors were connected to serve as an energy storage module. The wireless power transmission module consists of two electrical components, including a small rectifier and a receiving antenna with biodegradable Mo interconnects. When an external transmitting coil approaches, the alternating current (AC) input from the bioabsorbable Mg receiving coil was stabilized to DC power by a small rectifying circuit. The rectified DC output was used to charge the energy storage module while triggering the release of drug ions. The drug release device, the receiving rectifier module, and the energy storage units are interconnected in parallel. When wirelessly charging, the voltage applied to both ends of the drug

release device and supercapacitors remains consistent. After charging and then turning off the external input voltage, the energy storage module can effectively sustain the release of ionic drugs. The drug release stops when the external wireless charging is closed and all the electrical energy stored in the supercapacitors is exhausted. Achieving instant on and off of drug release is a very challenging problem that needs to be explored in depth. Although there is no instantaneous switching of drug release in the charging state, multiple triggering and dose control of drug release can be obtained in our proposed system. By controlling the on-off and duration of the input voltage at the transmitter chip, different sequential pulsating waveforms can be obtained (fig. S43). It would be important to explore the overall maintenance period of the energy harvested within the 5-min window and the proportion of time allocated to harvesting and charging. Therefore, we tested the voltage retention at both ends of the drug release device after 5 min of wireless charging. After removing the external transmitter chip, the discharge time of the supercapacitors applied to the drug release device can last up to 25 min (Fig. 7G). Unlike galvanostatic

charging, wireless charging of supercapacitors by rectified DC voltage is a passive constant-voltage charging process in which the actual voltage is initially lower than the measured voltage. The longer the voltage is applied to the positive and negative electrodes, the more sufficient the electrochemical reaction, resulting in more charge accumulated on its surface. Figure 7H shows the cumulative release of MB from a device after 1 hour of electrical stimulation with the integrated power system. This process is divided into five stages (I to V) of 15 min each, including two electrically triggered modes. For each stage, the first 5 min is triggered directly by a rectified DC voltage, while only the charged supercapacitors operate for the last 10 min. The synergistic triggering of the two modes results in the release of approximately 11.26 µg of MB within 1 hour, accounting for ~12.5% of the total drug mass. Because of the inherent defects of the supercapacitor itself, the voltage provided is constantly changing, and the drug release efficiency is lower than that of the wireless power supply alone. However, a short charge in the system can operate for a long time. On the other hand, by adjusting the wireless charging time, supercapacitors with different charging depths can be realized, thus playing the role of switches and achieving the purpose of on-demand energy release to a certain extent. To better play the advantages of the energy supply system, it is also urgent to develop strict switch control in the subsequent works. In contrast, the natural release of the ionic drug without electrical stimulation is negligible after 1 hour, which is consistent with the results above. Furthermore, the drug release device was placed between the porcine skin and the muscle tissue. In the absence of a voltage, the model drug remains inside the device and shows no sign of leakage. When a voltage is applied wirelessly, a large amount of model drugs is released from the device (Fig. 7I). Aside from the feasibility of ionic drugs, the drug delivery process can also be extended to nonionic drugs using ionic drugs that serve as carriers.

For in vivo drug delivery, we selected the IBU anionic model drug for controlled release. IBU is a nonsteroidal anti-inflammatory drug that can be used to reduce inflammation, relieve heat, and pain. Here, the antipyretic effects of the electrically triggered release of IBU were evaluated by yeast-induced fever in a rat model. Figure 8A illustrates a wireless energy supply and DDS implanted subcutaneously under the skin of a rat's back. The reservoirs in this case contain IBU hydrogel. Figure 8B and fig. S45 present photographs that show the site for implantation. The transmitter coil is placed over the implantation site to wirelessly power the implanted drug delivery device. The rectal temperatures of rats in each group before and after drug administration were recorded to monitor the body temperature changes. Rectal temperatures and their change value were recorded and measured at 0, 2, 4, 6, 8, 10, and 12 hours after drug administration. As shown in Fig. 8C, the rectal temperatures of the Model group (MG) were significantly higher than the No electrical stimulation drug release group (NG) and the Electronically controlled drug release group (E-DG), indicating that the yeast-induced pyretic model was successful after the drug administration; the rectal temperatures of E-DG decreased for about 4 hours. The results indicate that the successful release of electrically controlled IBU could reduce the rectal temperature in yeast-induced fever rats. We further analyzed enzyme-linked immunosorbent assay (ELISA) results of inflammatory factor interleukin-1β (IL-1β) and prostaglandin E2 (PGE2) in serum (Fig. 8, D and E). After drug administration, the level of IL-1β in E-DG decreased

significantly compared to MG ($P < 0.01$). The levels of PGE2 and E-DG could return to a normal level and showed statistical significance compared to MG. For the NG group, there is also a certain amount of passive drug released from the system, which could be attributed to two aspects. In addition to the differences in in vivo and in vitro water environment and circulation conditions, it is mainly due to the passive release of drugs driven by the concentration gradient after implantation. Hematoxylin and eosin (H&E) images of stained tissue sections collected appear in Fig. 8F and fig. S46, which indicates no damage to skin tissues and minimal to mild inflammatory cells related to implantation. Loose infiltrates of various inflammatory cells, including histiocytes, neutrophils, and fibroblasts, are observed in both the dermal and subcutaneous tissues (indicated by arrowheads). In the subcutaneous tissue, these inflammatory cells are accompanied by deposits of loosely arranged fibrous tissue, indicating a more structured inflammatory and reparative reaction to the implanted device (inset, square). All the results confirmed that the electrically controlled release of IBU drugs could reduce the level of proinflammatory factors in the serum of yeast-induced fever rats and has antipyretic and anti-inflammatory effects.

DISCUSSION

In summary, we developed a tissue-integrable, wireless power system for in vivo drug delivery that can not only instantaneously output DC voltage but also sustainably generate power for a certain period by an energy storage module. Our integrated device system exhibits favored tissue integrability, enabling it to conformally adhere to curved biological surfaces with minimal adverse effects on tissues for implantable uses, and eventually to undergo biodegradation within the body. The rational material and device designs result in high electrochemical performances for the energy storage module, as confirmed by a comprehensive study of the subtle structural evolution of electrode materials during the electrochemical degradation process. The wireless power supply system can be integrated with a compact, biodegradable, membrane-based drug delivery device, which can remotely control the drug release process. Our prototyped power supply system represents an important step forward in advancing a wide range of transient implantable bioelectronic devices with its potential to provide effective and reliable energy solutions.

MATERIALS AND METHODS
Fabrication of the Zn-MoS₂ hybrid supercapacitor

A facile one-step hydrothermal method was used to prepare MoS₂/rGO nanosheet array on Mo foil (act as substrate and Mo source). Typically, Mo foil (20 µm for electrochemical characterizations and 10 µm for dissolution tests, 99.99% trace metal basis) was cut into 1 cm × 4 cm pieces and cleaned with 1 M HCl, followed by ultrasonication for 20 min in acetone, deionized (DI) water, and ethanol, respectively. A 30-ml aqueous solution containing 0.5 M thiourea (1.14 g) and 2 ml of graphene oxide (GO) (3.33 mg/ml) was prepared through an ultrasonication treatment for 30 min and then transferred into a 50-ml Teflon-lined autoclave. The as-prepared Mo foil was placed against the bottom (at an angle of 45°). Thereinto, GO was synthesized using a modified Hummers's method (79). Last, the autoclave was heated to 180°C for a time period of
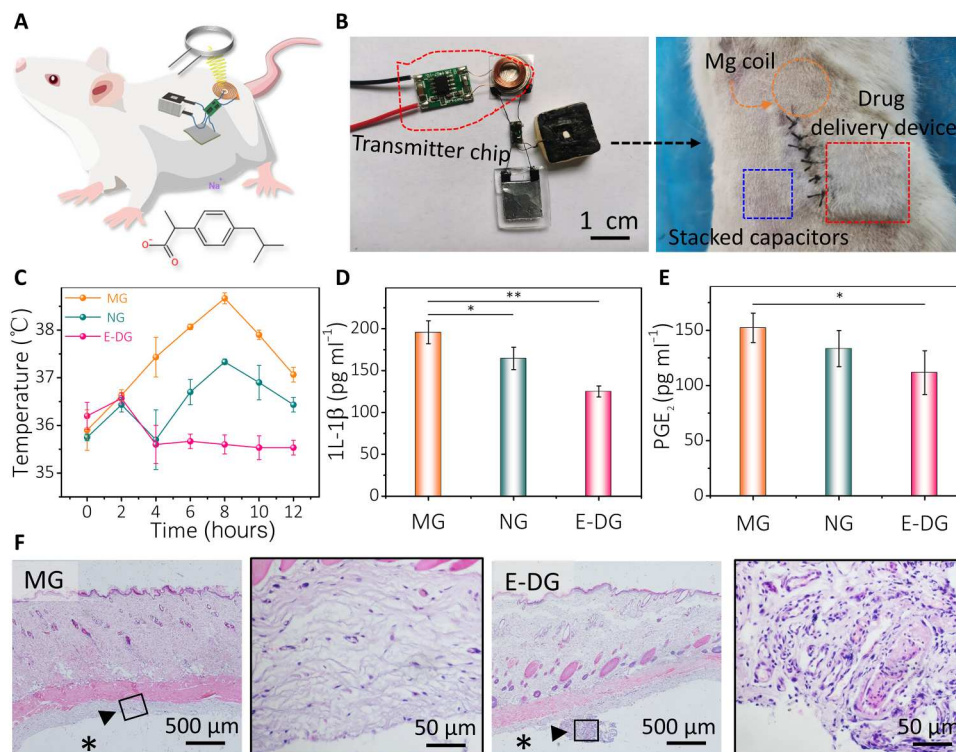
Fig. 8. In vivo studies of controlled drug release of IBU under the skin of the rat back. (**A**) Illustration of the placement of an integrated power system with drug delivery device to the subcutaneous dorsal. (**B**) Photographs of an implanted device. (**C**) Rectal temperatures change value at 0, 2, 4, 6, 8, 10, and 12 hours after yeast administration. Effects of released IBU on the production of (**D**) IL-1β and (**E**) PGE2 (n = 3). *P < 0.05, **P < 0.01, versus MG. (**F**) Representative images of H&E-stained cross-sectional areas near the implantation site of control (MG) and full devices (E-DG). Subcutaneous cavitation corresponds to the device implantation site (asterisk). A mixture of loosely infiltrated inflammatory cells can be seen in the dermal and subcutaneous tissues (arrowheads). Inflammatory cells in the subcutaneous tissue are composed of histiocytes, neutrophils, and fibroblasts (inset, square).

24 hours. In comparison, the pristine Mo cathode was obtained without adding GO solution in a similar hydrothermal reaction. The freestanding Alg-Zn electrolyte film was prepared by a facile ionic cross-linking reaction. Initially, 0.8 g of sodium alginate powder (AR grade, Sigma-Aldrich) was dissolved into 20 ml of DI water followed by continuous agitation in a water bath at 85°C. After the solution became colorless or transparent, it was stored at room temperature for 24 hours to remove the produced bubbles. The obtained sodium alginate solution was poured into a carved polyethylene terephthalate (PET) mold with a thickness of about 100 μm and then immersed into 1 M $ZnCl_2$ solution over 24 hours to achieve the ultimate Alg-Zn electrolyte film. The obtained Alg-Zn electrolyte film was peeled off and cut into a size of 1 cm × 1 cm square. The sandwiched Zn-MoS$_2$ hybrid supercapacitor was assembled by stacking the electrodes [MoS$_2$/rGO cathode, Zn foil (0.02 mm, 99.99% trace metal basis) anode] and Alg-Zn electrolyte film layer by layer. One side of the electrodes was connected to a copper tape with silver paste. A mild pressure was applied on both sides for another 10 min before the tests.

Fabrication of the magnetic induction coil
In a typical process, a piece of Mg foil (thickness, ~20 μm) was first attached to a poly(dimethylsiloxane) (9:1) slab. The coil structure was generated by using a controllable laser ablation technique. After thorough ablation, the patterned Mg coil (size, 1.2 cm × 1.2

cm) was transferred onto a preformed PLGA [~30 μm thick, 65:35 (lactide: glycolide); Jinan Daigang Biomaterial Co. Ltd., China] substrate by soaking with a drop of ethyl acetate for about 1 min.

Integration of Mg receiver with energy storage unit
The energy storage unit consists of four biodegradable Zn-MoS$_2$ hybrid supercapacitors in series and highly conductive Ag interconnections with a fractal serpentine pattern. An island-bridge structure was designed and fabricated on a soft and bioresorbable substrate composed of PLLA-PTMC (30:70) (Jinan Daigang Biomaterial Co. Ltd., China) to maximize the mechanical robustness of the interconnects. A two-by-two array of Zn-MoS$_2$ hybrid supercapacitors was attached to a PLLA-PTMC film as "islands" while Ag interconnections were screen-printed in serpentine patterns as "bridges." For in vivo and degradation tests, this part was replaced with a laser-cutting Mg foil (thickness, 20 μm). Zn-ion hybrid supercapacitors were connected to the Mg electrode with the assistance of the biodegradable conductive tungsten(W) paste (*80*). Their surfaces and edges were encapsulated with PLGA. A mini wireless charging module (XKT 510-04) was purchased from Shenzhen Xinketai Semiconductor Co. Ltd. The transmitter module features a volume size of 11 mm × 17 mm, with a weight of 1.2 g. A rectifier circuit (size, 4 mm × 7 mm; weight, 75 mg) was used to stabilize the AC input from the Mg coil interconnected with a

bioresorbable Mo wire. Last, the top was covered with a layer of PLLA-PTMC.

Fabrication of the drug delivery device

The electrically triggered drug delivery device consists of a top electrode, a separation membrane, a drug reservoir, and a bottom electrode. First, a drug reservoir with a 1-mm-diameter pinhole was made by compressing hot PLA melt on a stainless steel mask (see the Supplementary Materials). The main body of the reservoir is a hollow cylinder with a diameter of 3 mm and a height of 3 mm. The MCE membrane with a 5-μm pore size was purchased from Shanghai Xingya, China. A circular membrane of 2 mm in diameter was cut and placed above the pinhole and thermally glued to the reservoir. Then, a top electrode was screen-printed on the PLA reservoir surface with carbon paste, followed by injecting 90 μl of drug-containing gel into the reservoir. The blank hydrogel was prepared by mixing 2 weight % xanthan gum powder (USP grade, Macklin) with PBS solution (0.1 M, pH 7.4) at room temperature. Ten-milligram MB powder was then dissolved in 10 ml of blank hydrogel as the cationic drug for the drug release test. Next, a PLA film with a screen-printed carbon bottom electrode was sealed underneath the reservoir. Last, biodegradable Mo wires were used to connect the electrodes to an external power source for the drug release test. To prevent the leakage of drug ions, the device was uniformly encapsulated with a molten mixture of refined beeswax and candelilla wax at a weight ratio of 2:3 at 85°C before use. The thickness of the encapsulation layer can be proportionally controlled by the cycles of dipping. In comparison, devices containing anionic drug (IBU) was prepared in a similar process. For drug release in vivo, larger reservoirs are designed for use, with detailed dimensions given in the Supplementary Materials (fig. S44). The concentration of IBU in the drug gel was elevated to 0.1 g ml^{-1}.

Drug release test

The biodegradable drug delivery device was immersed in a plastic vial containing 4 ml of fresh PBS solution. All drug release experiments were performed at room temperature and repeated at least three times to check the repeatability. The required constant DC voltage was applied to the device with a DC power supply or our Zn-MoS$_2$ hybrid supercapacitor array. After certain time intervals, the PBS solution was replaced with a fresh batch. The released drug concentration in the old PBS batch was then measured by an ultraviolet-visible (UV-vis) spectrophotometer (U-3900H, HITACHI). Concentrations of MB and IBU were determined by a typical absorption peak at 665 and 222 nm, respectively.

Biodegradation evaluation

The as-prepared Zn-MoS$_2$ hybrid supercapacitors (1 cm × 1 cm) were encapsulated with wax and soaked in a petri dish with PBS solution (0.1 M, pH 7.4) at an elevated temperature (85°C) in an incubator. The PBS solution in the petri dish was replaced every day. Time-series images were taken at various stages. The dissolution test of the integrated power system was similar to the procedure described above.

Mechanical simulation

The finite element analysis (FEA) commercial software ABAQUS was used to study the strain level of the wireless energy-harvesting and storage device under bending and twisting. Since the thickness of each layer of the device is thin as shown in Fig. 1B, the shell elements (S4R) were used for modeling. The minimal element size was one-fourth of the width of the Mg interconnects (200 μm), which ensured the convergence and the accuracy of the simulation results. The elastic modulus (E) and Poisson′s ratio (ν) used in the analysis were $E_{Mg} = 45$ GPa and $ν_{Mg} = 0.35$ for Mg, $E_{Zn} = 96.5$ GPa and $ν_{Zn} = 0.3$ for zinc, $E_{Mo} = 320$ GPa and $ν_{Mo} = 0.38$ for molybdenum, $E_{Alg-Zn} = 7.21$ GPa and $ν_{Alg-Zn} = 0.3$ for Alg-Zn, and $E_{PLLA-PTMC} = 163$ kPa and $ν_{PLLA-PTMC} = 0.35$ for PLLA-PTMC.

Material characterization

The morphology and microstructures were observed on field-emission SEM (FEI-SEM, Apreo S), TEM, and SAED patterns (FEI Tecnai F30, at 300 kV). The crystal structures were achieved by XRD in the 2θ range of 10° to 90° (Philips, X′pert pro, Cu Kα, 0.15406 nm) and Raman spectroscopy (JY-HR800 micro-Raman, using a 532-nm wavelength YAG laser). The chemical compositions of the MoS$_2$/rGO cathode were investigated by using XPS (PHI-5702, Mg KR x-ray, 1253.6 eV). Information about chemical bonds or functional groups of the electrolyte films was analyzed by an FTIR spectrometer (Nicolet 6700). TGA was performed on a PerkinElmer termogravimetry (TG)/differential thermal analysis (DTA) with a heating rate of 10°C min^{-1} in an air atmosphere. The thickness of the Alg-Zn electrolyte and Zn-MoS$_2$ hybrid supercapacitor was measured by a helical micrometer with a precision of 0.001 mm.

Electrochemical measurement

Zn plating/stripping measurements were examined by a multichannel battery test system (LAND CT2001A, China). CV and GCD examinations were carried out on an electrochemical workstation (CHI 660E) to analyze the electrochemical behavior and the rate performance of the Zn-Mo hybrid supercapacitor. Electrochemical impedance spectroscopy (EIS) was conducted at the open-circuit potential with frequencies ranging from 0.1 Hz to 100 kHz. The electrochemical properties of aqueous Zn-MoS$_2$ hybrid supercapacitors were tested in a two-electrode system in a 1 M ZnCl$_2$ electrolyte.

Cell cytotoxicity

Cell viability and cell death were evaluated by using CCK-8 assay and calcein-AM/PI staining, respectively. The NIH/3T3 mouse embryonic fibroblast cells were harvested during the logarithmic growth phase, digested with trypsin, and centrifuged to form a single-cell suspension. The suspended cells ($1 × 10^4$ cells per well) were seeded on material surfaces and maintained in Dulbecco′s modified Eagle′s medium (Gibco) with 10% fetal bovine serum (Gibco) and 1% penicillin/streptomycin (Gibco). First, pure Mo foil and MoS$_2$/rGO electrodes (3 mm × 3 mm) sterilized by DI water, alcohol, and UV light were fixed on the bottom of a 12-well culture plate and incubated in a cell incubator with a humidity atmosphere containing 5% CO$_2$ at 37°C. After incubation for 24, 48, and 120 hours, 100 μl of CCK-8 solution was added to each well to detect the cell viability. A multimode microplate reader (Bio-Rad, USA) was used to measure the optical density value at 450 nm. Three parallel control cells were applied to each group. Meanwhile, after CCK-8 reagents were removed, the cells were washed using PBS twice at room temperature and then stained with calcein-AM

and PI, respectively. Fluorescence images were obtained by fluorescence microscopy (U-LH50HG, Olympus, Japan).

In vivo degradation tests

The male SD rats (white, 160 to 200 g, 40 days) were purchased from the Animal Center of Medical College of Lanzhou University (China). They were housed in a temperaturecontrolled environment ($22 \pm 1°C$), exposed to a 12-hour light/dark cycle, and allowed food and water ad libitum. Animals were used only once and received high-quality humane treatment. Before the surgery, the PLGA-encapsulated Zn-MoS$_2$ hybrid supercapacitors were sterilized by UV and 75% alcohol and implanted subcutaneously in the back of SD rats. To demonstrate biocompatibility and in vivo degradation, the rats were sacrificed and dissected at the time of 2, 4, 6, and 8 weeks after implantation. H&E staining was performed on frozen sections of different organs and tissues around the implantation site.

In vivo electronically controlled drug delivery and model construction

Similar to the aforementioned in vivo degradation tests, the SD rats were acclimated for 1 week in their housing conditions. Nine healthy male rats were selected and randomly divided into three groups: MG ($n = 3$), NG ($n = 3$), and E-DG ($n = 3$). For the MG, a complete drug release device was implanted under the skin of the rat's back. For an E-DG, an integrated energy supply system was connected to a drug delivery device and implanted beneath the rat's skin on its back. After a week, the wounds in the group where the device was implanted were observed to have healed effectively, and the sutures were removed. The foreign body response might affect drug delivery process, which could be mitigated through pharmacological strategies. The local inflammatory response resulting from the device implantation was alleviated by administering IBU sodium orally. Subsequently, for three consecutive days, the drug release device on the rat's back was electrically stimulated for approximately 1 hour each day. This stimulation included both wireless charging to provide a direct energy supply and the use of supercapacitors for an auxiliary energy supply after charging. The purpose of this stimulation was to enhance the release of IBU from the device inside the rat's body. Following the completion of the final electrical trigger to release IBU, a subcutaneous injection of 20% yeast water suspension (10 ml/kg) was administered into the rats' back. After half an hour, rectal temperature measurements were taken at 0, 2, 4, 6, 8, 10, and 12 hours after the yeast injection using a digital thermometer.

Sample collection and cytokines

After the final rectal temperature measurement, all rats were anesthetized through peritoneal injection of pentobarbital sodium. The blood from the abdominal aorta was promptly collected in heparinized tubes. After allowing it to stand for 1 hour, the tubes were centrifuged at 3000 rpm for 10 min, resulting in the separation of the supernatant, which was then stored in a refrigerator at −80°C. To measure the levels of cytokines in the serum, IL-1β and PGE2 ELISA kits (nos. ER1094 and ER1800, Wuhan Fine Biotech, China) were used, following the instructions provided by the manufacturer. This involved diluting the standard product, adding the samples, performing washes, and terminating the color reaction. The standard product well served as the experimental reference, and the absorbance of each well was measured at a wavelength of 450 nm using a microplate reader. A standard concentration curve was plotted to calculate the concentrations of IL-1β and PGE2 in the serum.

Ethical statement

We followed the protocol approved by the Ethics Committee of Lanzhou University (approval reference no. LZUKQ-2023-025). Animal care was in accordance with the institutional guidelines of Lanzhou University (China). Protocols were proved by the Institutional Animal Care and Use Committee at Lanzhou University.

REFERENCES AND NOTES

1. H. Lee, Y. Lee, C. Song, H. R. Cho, R. Ghaffari, T. K. Choi, K. H. Kim, Y. B. Lee, D. Ling, H. Lee, S. J. Yu, S. H. Choi, T. Hyeon, D.-H. Kim, An endoscope with integrated transparent bioelectronics and theranostic nanoparticles for colon cancer treatment. *Nat. Commun.* **6**, 10059 (2015).

2. D. Seo, R. M. Neely, K. Shen, U. Singhal, E. Alon, J. M. Rabaey, J. M. Carmena, M. M. Maharbiz, Wireless recording in the peripheral nervous system with ultrasonic neural dust. *Neuron* **91**, 529–539 (2016).

3. H. Ouyang, Z. Liu, N. Li, B. Shi, Y. Zou, F. Xie, Y. Ma, Z. Li, H. Li, Q. Zheng, X. Qu, Y. Fan, Z. L. Wang, H. Zhang, Z. Li, Symbiotic cardiac pacemaker. *Nat. Commun.* **10**, 1821 (2019).

4. L. Wang, C. Lu, S. Yang, P. Sun, Y. Wang, Y. Guan, S. Liu, D. Cheng, H. Meng, Q. Wang, J. He, H. Hou, H. Li, W. Lu, Y. Zhao, J. Wang, Y. Zhu, Y. Li, D. Luo, T. Li, H. Chen, S. Wang, X. Sheng, W. Xiong, X. Wang, J. Peng, L. Yin, A fully biodegradable and self-electrified device for neuroregenerative medicine. *Sci. Adv.* **6**, eabc6686 (2020).

5. K. Sim, F. Ershad, Y. Zhang, P. Yang, H. Shim, Z. Rao, Y. Lu, A. Thukral, A. Elgalad, Y. Xi, B. Tian, D. A. Taylor, C. Yu, An epicardial bioelectronic patch made from soft rubbery materials and capable of spatiotemporal mapping of electrophysiological activity. *Nat. Electron.* **3**, 775–784 (2020).

6. J. T. Reeder, Z. Xie, Q. Yang, M.-H. Seo, Y. Yan, Y. Deng, K. R. Jinkins, S. R. Krishnan, C. Liu, S. McKay, E. Patnaude, A. Johnson, Z. Zhao, M. J. Kim, Y. Xu, I. Huang, R. Avila, C. Felicelli, E. Ray, X. Guo, W. Z. Ray, Y. Huang, M. R. MacEwan, J. A. Rogers, Soft, bioresorbable coolers for reversible conduction block of peripheral nerves. *Science* **377**, 109–115 (2022).

7. H. Dinis, P. M. Mendes, A comprehensive review of powering methods used in state-of-the-art miniaturized implantable electronic devices. *Biosens. Bioelectron.* **172**, 112781 (2021).

8. T. Ye, J. Wang, Y. Jiao, L. Li, E. He, L. Wang, Y. Li, Y. Yun, D. Li, J. Lu, H. Chen, Q. Li, F. Li, R. Gao, H. Peng, Y. Zhang, A tissue-like soft all-hydrogel battery. *Adv. Mater.* **34**, 2105120 (2021).

9. S. He, S. Hu, J. Wan, Q. Gao, Y. Wang, S. Xie, L. Qiu, C. Wang, G. Zheng, B. Wang, H. Peng, Biocompatible carbon nanotube fibers for implantable supercapacitors. *Carbon* **122**, 162–167 (2017).

10. G. Lee, S.-K. Kang, S. M. Won, P. Gutruf, Y. R. Jeong, J. Koo, S.-S. Lee, J. A. Rogers, J. S. Ha, Fully biodegradable microsupercapacitor for power storage in transient electronics. *Adv. Energy Mater.* **7**, 1700157 (2017).

11. X. Huang, D. Wang, Z. Yuan, W. Xie, Y. Wu, R. Li, Y. Zhao, D. Luo, L. Cen, B. Chen, H. Wu, H. Xu, X. Sheng, M. Zhang, L. Zhao, L. Yin, A fully biodegradable battery for self-powered transient implants. *Small* **14**, e1800994 (2018).

12. H. Li, C. Zhao, X. Wang, J. Meng, Y. Zou, S. Noreen, L. Zhao, Z. Liu, H. Ouyang, P. Tan, M. Yu, Y. Fan, Z. L. Wang, Z. Li, Fully bioabsorbable capacitor as an energy storage unit for implantable medical electronics. *Adv. Sci.* **6**, 1801625 (2019).

13. H. Lee, G. Lee, J. Yun, K. Keum, S. Y. Hong, C. Song, J. W. Kim, J. H. Lee, S. Y. Oh, D. S. Kim, M. S. Kim, J. S. Ha, Facile fabrication of a fully biodegradable and stretchable serpentine-shaped wire supercapacitor. *Chem. Eng. J.* **366**, 62–71 (2019).

14. H. Sheng, J. Zhou, B. Li, Y. He, X. Zhang, J. Liang, J. Zhou, Q. Su, E. Xie, W. Lan, K. Wang, C. Yu, A thin, deformable, high-performance supercapacitor implant that can be biodegraded and bioabsorbed within an animal body. *Sci. Adv.* **7**, eabe3097 (2021).

15. J. Zhou, R. Zhang, R. Xu, Y. Li, W. Tian, M. Gao, M. Wang, D. Li, X. Liang, L. Xie, K. Liang, P. Chen, B. Kong, Super-assembled hierarchical cellulose aerogel-gelatin solid electrolyte for implantable and biodegradable zinc ion battery. *Adv. Funct. Mater.* **32**, 2111406 (2022).

16. I. Huang, Y. Zhang, H. M. Arafa, S. Li, A. Vazquez-Guardado, W. Ouyang, F. Liu, S. Madhvapathy, J. W. Song, A. Tzavelis, J. Trueb, Y. Choi, W. J. Jeang, V. Forsberg, E. Higbee-Dempsey, N. Ghoreishi-Haack, I. Stepien, K. Bailey, S. Han, Z. J. Zhang, C. Good, Y. Huang, A. J. Bandodkar, J. A. Rogers, High performance dual-electrolyte magnesium–iodine batteries that can harmlessly resorb in the environment or in the body. *Energy Environ. Sci.* **15**, 4095–4108 (2022).

17. M. Shao, H. Sheng, L. Lin, H. Ma, Q. Wang, J. Yuan, X. Zhang, G. Chen, W. Li, Q. Su, E. Xie, J. Wang, Z. Zhang, W. Lan, High-performance biodegradable energy storage devices enabled by heterostructured MoO₃–MoS₂ composites. *Small* **19**, e2205529 (2023).

18. X. Huang, H. Hou, B. Yu, J. Bai, Y. Guan, L. Wang, K. Chen, X. Wang, P. Sun, Y. Deng, S. Liu, X. Cai, Y. Wang, J. Peng, X. Sheng, W. Xiong, L. Yin, Fully biodegradable and long-term operational primary zinc batteries as power sources for electronic medicine. *ACS Nano* **17**, 5727–5739 (2023).

19. S. Yoo, J. Lee, H. Joo, S.-H. Sunwoo, S. Kim, D.-H. Kim, Wireless power transfer and telemetry for implantable bioelectronics. *Adv. Healthc. Mater.* **10**, e2100614 (2021).

20. H. Sheng, X. Zhang, J. Liang, M. Shao, E. Xie, C. Yu, W. Lan, Recent advances of energy solutions for implantable bioelectronics. *Adv. Healthc. Mater.* **10**, 2100199 (2021).

21. Q. Guo, J. Koo, Z. Xie, R. Avila, X. Yu, X. Ning, H. Zhang, X. Liang, S. B. Kim, Y. Yan, M. R. MacEwan, H. M. Lee, A. Song, Z. Di, Y. Huang, Y. Mei, J. A. Rogers, A bioresorbable magnetically coupled system for low-frequency wireless power transfer. *Adv. Funct. Mater.* **29**, 1905451 (2019).

22. X. Huang, H. Li, J. Li, L. Huang, K. Yao, C. K. Yiu, Y. Liu, T. H. Wong, D. Li, M. Wu, Y. Huang, Z. Gao, J. Zhou, Y. Gao, J. Li, Y. Jiao, R. Shi, B. Zhang, B. Hu, Q. Guo, E. Song, R. Ye, X. Yu, Transient, implantable, ultrathin biofuel cells enabled by laser-induced graphene and gold nanoparticles composite. *Nano Lett.* **22**, 3447–3456 (2022).

23. D. Jiang, B. Shi, H. Ouyang, Y. Fan, Z. L. Wang, Z. Li, Emerging implantable energy harvesters and self-powered implantable medical electronics. *ACS Nano* **14**, 6436–6448 (2020).

24. W. Deng, Y. Zhou, A. Libanori, G. Chen, W. Yang, J. Chen, Piezoelectric nanogenerators for personalized healthcare. *Chem. Soc. Rev.* **51**, 3380–3435 (2022).

25. K. Song, J. H. Han, T. Lim, N. Kim, S. Shin, J. Kim, H. Choo, S. Jeong, Y. C. Kim, Z. L. Wang, J. Lee, Subdermal flexible solar cell arrays for powering medical electronic implants. *Adv. Healthc. Mater.* **5**, 1572–1580 (2016).

26. L. Lu, Z. Yang, K. Meacham, C. Cvetkovic, E. A. Corbin, A. Vázquez-Guardado, M. Xue, L. Yin, J. Boroumand, G. Pakeltis, T. Sang, K. J. Yu, D. Chanda, R. Bashir, R. W. Gereau Iv, X. Sheng, J. A. Rogers, Biodegradable monocrystalline silicon photovoltaic microcells as power supplies for transient biomedical implants. *Adv. Energy Mater.* **8**, 1703035 (2018).

27. J. Kim, J. Seo, D. Jung, T. Lee, H. Ju, J. Han, N. Kim, J. Jeong, S. Cho, J. H. Seol, J. Lee, Active photonic wireless power transfer into live tissues. *Proc. Natl. Acad. Sci. U.S.A.* **117**, 16856–16863 (2020).

28. S. M. Won, L. Cai, P. Gutruf, J. A. Rogers, Wireless and battery-free technologies for neuroengineering. *Nat. Biomed. Eng.* **7**, 405–423 (2023).

29. M. Yu, Y. Peng, X. Wang, F. Ran, Emerging design strategies toward developing next-generation implantable batteries and supercapacitors. *Adv. Funct. Mater.* **33**, 2301877 (2023).

30. E. G. da Silveira Firmiano, A. C. Rabelo, C. J. Dalmaschio, A. N. Pinheiro, E. C. Pereira, W. H. Schreiner, E. R. Leite, Supercapacitor electrodes obtained by directly bonding 2D MoS₂ on reduced graphene oxide. *Adv. Energy Mater.* **4**, 1301380 (2014).

31. X. Xie, J. Li, Z. Xing, B. Lu, S. Liang, J. Zhou, Biocompatible zinc battery with programmable electro-cross-linked electrolyte. *Natl. Sci. Rev.* **10**, nwac281 (2022).

32. X. Chen, Y. J. Park, M. Kang, S.-K. Kang, J. Koo, S. M. Shinde, J. Shin, S. Jeon, G. Park, Y. Yan, M. R. MacEwan, W. Z. Ray, K.-M. Lee, J. A. Rogers, J.-H. Ahn, CVD-grown monolayer MoS₂ in bioabsorbable electronics and biosensors. *Nat. Commun.* **9**, 1690 (2018).

33. T. Sun, Z. Li, X. Liu, L. Ma, J. Wang, S. Yang, Oxygen-incorporated MoS₂ microspheres with tunable interiors as novel electrode materials for supercapacitors. *J. Power Sources* **352**, 135–142 (2017).

34. K. D. Rasamani, F. Alimohammadi, Y. Sun, Interlayer-expanded MoS₂. *Mater. Today* **20**, 83–91 (2017).

35. K. Krishnamoorthy, G. K. Veerasubramani, P. Pazhamalai, S. J. Kim, Designing two dimensional nanoarchitectured MoS₂ sheets grown on Mo foil as a binder free electrode for supercapacitors. *Electrochim. Acta* **190**, 305–312 (2016).

36. Y. Zhou, Q. Bao, L. A. L. Tang, Y. Zhong, K. P. Loh, Hydrothermal dehydration for the "green" reduction of exfoliated graphene oxide to graphene and demonstration of tunable optical limiting properties. *Chem. Mater.* **21**, 2950–2956 (2009).

37. C. Lee, H. Yan, L. E. Brus, T. F. Heinz, J. Hone, S. Ryu, Anomalous lattice vibrations of single- and few-layer MoS₂. *ACS Nano* **4**, 2695–2700 (2010).

38. A. C. Ferrari, J. Robertson, Interpretation of Raman spectra of disordered and amorphous carbon. *Phys. Rev. B* **61**, 14095–14107 (2000).

39. M. A. Pimenta, G. Dresselhaus, M. S. Dresselhaus, L. G. Cançado, A. Jorio, R. Saito, Studying disorder in graphite-based systems by Raman spectroscopy. *Phys. Chem. Chem. Phys.* **9**, 1276–1290 (2007).

40. Y.-J. Tang, Y. Wang, X.-L. Wang, S.-L. Li, W. Huang, L.-Z. Dong, C.-H. Liu, Y.-F. Li, Y.-Q. Lan, Molybdenum disulfide/nitrogen-doped reduced graphene oxide nanocomposite with enlarged interlayer spacing for electrocatalytic hydrogen evolution. *Adv. Energy Mater.* **6**, 1600116 (2016).

41. Q. Liu, Q. Fang, W. Chu, Y. Wan, X. Li, W. Xu, M. Habib, S. Tao, Y. Zhou, D. Liu, T. Xiang, A. Khalil, X. Wu, M. Chhowalla, P. M. Ajayan, L. Song, Electron-doped 1T-MoS₂ via interface engineering for enhanced electrocatalytic hydrogen evolution. *Chem. Mater.* **29**, 4738–4744 (2017).

42. Y. Li, K. Yin, L. Wang, X. Lu, Y. Zhang, Y. Liu, D. Yan, Y. Song, S. Luo, Engineering MoS₂ nanomesh with holes and lattice defects for highly active hydrogen evolution reaction. *Appl. Catal. B Environ.* **239**, 537–544 (2018).

43. D. Sarkar, D. Das, S. Das, A. Kumar, S. Patil, K. K. Nanda, D. D. Sarma, A. Shukla, Expanding interlayer spacing in MoS₂ for realizing an advanced supercapacitor. *ACS Energy Lett.* **4**, 1602–1609 (2019).

44. T.-T. Shan, S. Xin, Y. You, H.-P. Cong, S.-H. Yu, A. Manthiram, Combining nitrogen-doped graphene sheets and MoS₂: A unique film-foam-film structure for enhanced lithium storage. *Angew. Chem. Int. Ed.* **55**, 12783–12788 (2016).

45. J. Xie, J. Zhang, S. Li, F. Grote, X. Zhang, H. Zhang, R. Wang, Y. Lei, B. Pan, Y. Xie, Controllable disorder engineering in oxygen-incorporated MoS₂ ultrathin nanosheets for efficient hydrogen evolution. *J. Am. Chem. Soc.* **135**, 17881–17888 (2013).

46. X. Fan, C. Zhong, J. Liu, J. Ding, Y. Deng, X. Han, L. Zhang, W. Hu, D. P. Wilkinson, J. Zhang, Opportunities of flexible and portable electrochemical devices for energy storage: Expanding the spotlight onto semi-solid/solid electrolytes. *Chem. Rev.* **122**, 17155–17239 (2022).

47. Y. Tang, C. Liu, H. Zhu, X. Xie, J. Gao, C. Deng, M. Han, S. Liang, J. Zhou, Ion-confinement effect enabled by gel electrolyte for highly reversible dendrite-free zinc metal anode. *Energy Storage Mater.* **27**, 109–116 (2020).

48. D. Leal, B. Matsuhiro, M. Rossi, F. Caruso, FT-IR spectra of alginic acid block fractions in three species of brown seaweeds. *Carbohydr. Res.* **343**, 308–316 (2008).

49. T. S. Pathak, J.-H. Yun, S.-J. Lee, D.-J. Baek, K.-J. Paeng, Effect of cross-linker and cross-linker concentration on porosity, surface morphology and thermal behavior of metal alginates prepared from algae (Undaria pinnatifida). *Carbohydr. Polym.* **78**, 717–724 (2009).

50. Y. Zeng, X. Zhang, Y. Meng, M. Yu, J. Yi, Y. Wu, X. Lu, Y. Tong, Achieving ultrahigh energy density and long durability in a flexible rechargeable quasi-solid-state Zn–MnO₂ battery. *Adv. Mater.* **29**, 1700274 (2017).

51. S. Zhang, N. Yu, S. Zeng, S. Zhou, M. Chen, J. Di, Q. Li, An adaptive and stable bio-electrolyte for rechargeable Zn-ion batteries. *J. Mater. Chem. A* **6**, 12237–12243 (2018).

52. Y. Huang, J. Zhang, J. Liu, Z. Li, S. Jin, Z. Li, S. Zhang, H. Zhou, Flexible and stable quasi-solid-state zinc ion battery with conductive guar gum electrolyte. *Mater. Today Energy* **14**, 100349 (2019).

53. J. Evans, C. A. Vincent, P. G. Bruce, Electrochemical measurement of transference numbers in polymer electrolytes. *Polymer* **28**, 2324–2328 (1987).

54. H. Li, Z. Tang, Z. Liu, C. Zhi, Evaluating flexibility and wearability of flexible energy storage devices. *Joule* **3**, 613–619 (2019).

55. S. Wang, M. Li, J. Wu, D.-H. Kim, N. Lu, Y. Su, Z. Kang, Y. Huang, J. A. Rogers, Mechanics of epidermal electronics. *J. Appl. Mech.* **79**, 031022 (2012).

56. S. Ardizzone, G. Fregonara, S. Trasatti, Inner and outer active surface of RuO₂ electrodes. *Electrochim. Acta* **35**, 263–267 (1990).

57. J. Liu, J. Wang, C. Xu, H. Jiang, C. Li, L. Zhang, J. Lin, Z. X. Shen, Advanced energy storage devices: Basic principles, analytical methods, and rational materials design. *Adv. Sci.* **5**, 1700322 (2018).

58. X. Wang, W. Xu, P. Chatterjee, C. Lv, J. Popovich, Z. Song, L. Dai, M. Y. S. Kalani, S. E. Haydel, H. Jiang, Food-materials-based edible supercapacitors. *Adv. Mater. Technol.* **1**, 1600059 (2016).

59. M. Hu, J. Wang, J. Liu, P. Wang, Y. Feng, H. Wang, N. Nie, Y. Wang, Y. Huang, A flour-based one-stop supercapacitor with intrinsic self-healability and stretchability after self-healing and biodegradability. *Energy Storage Mater.* **21**, 174–179 (2019).

60. W. Tian, Y. Li, J. Zhou, T. Wang, R. Zhang, J. Cao, M. Luo, N. Li, N. Zhang, H. Gong, J. Zhang, L. Xie, B. Kong, Implantable and biodegradable micro-supercapacitor based on a super-assembled three-dimensional network Zn@PPy hybrid electrode. *ACS Appl. Mater. Interfaces* **13**, 8285–8293 (2021).

61. M. B. Durukan, M. O. Cicek, D. Doganay, M. C. Gorur, S. Çınar, H. E. Unalan, Multifunctional and physically transient supercapacitors, triboelectric nanogenerators, and capacitive sensors. *Adv. Funct. Mater.* **32**, 2106066 (2021).

62. X. Yang, H. Niu, H. Jiang, Q. Wang, F. Qu, A high energy density all-solid-state asymmetric supercapacitor based on MoS$_2$/graphene nanosheets and MnO$_2$/graphene hybrid electrodes. *J. Mater. Chem. A* **4**, 11264–11275 (2016).

63. W. Yang, L. He, X. Tian, M. Yan, H. Yuan, X. Liao, J. Meng, Z. Hao, L. Mai, Carbon-MEMS-based alternating stacked MoS$_2$@rGO-CNT micro-supercapacitor with high capacitance and energy density. *Small* **13**, 1700639 (2017).

64. W. Xu, C. Sun, K. Zhao, X. Cheng, S. Rawal, Y. Xu, Y. Wang, Defect engineering activating (Boosting) zinc storage capacity of MoS$_2$. *Energy Storage Mater.* **16**, 527–534 (2019).

65. S. M. Yang, J. H. Shim, H.-U. Cho, T.-M. Jang, G.-J. Ko, J. Shim, T. H. Kim, J. Zhu, S. Park, Y. S. Kim, S.-Y. Joung, J. C. Choe, J.-W. Shin, J. H. Lee, Y. M. Kang, H. Cheng, Y. Jung, C.-H. Lee, D. P. Jang, S.-W. Hwang, Hetero-integration of silicon nanomembranes with 2D materials for bioresorbable, wireless neurochemical system. *Adv. Mater.* **34**, 2108203 (2022).

66. T. Fan, L. Yan, S. He, Q. Hong, F. Ai, S. He, T. Ji, X. Hu, E. Ha, B. Zhang, Z. Li, H. Zhang, X. Chen, J. Hu, Biodistribution, degradability and clearance of 2D materials for their biomedical applications. *Chem. Soc. Rev.* **51**, 7732–7751 (2022).

67. Q. Lv, X. Li, X. Tian, D. Fu, H. Liu, J. Liu, Y. Song, B. Cai, J. Wang, Q. Su, W. Chen, M. Zou, F. Xiao, S. Wang, Z. Wang, L. Wang, A degradable and biocompatible supercapacitor implant based on functional sericin hydrogel electrode. *Adv. Energy Mater.* **13**, 2203814 (2023).

68. Y. Choi, J. Koo, J. A. Rogers, Inorganic materials for transient electronics in biomedical applications. *MRS Bull.* **45**, 103–112 (2020).

69. K. V. Rajagopalan, Molybdenum: An essential trace-element in human-nutrition. *Annu. Rev. Nutr.* **8**, 401–427 (1988).

70. K. Jeejeebhoy, Zinc: An essential trace element for parenteral nutrition. *Gastroenterology* **137**, S7–S12 (2009).

71. X. Xie, J. Li, Z. Xing, B. Lu, S. Liang, J. Zhou, Biocompatible zinc battery with programmable electro-crosslinked electrolyte. *Natl. Sci. Rev.* **10**, nwac281 (2022).

72. C. Li, C. Guo, V. Fitzpatrick, A. Ibrahim, M. J. Zwierstra, P. Hanna, A. Lechtig, A. Nazarian, S. J. Lin, D. L. Kaplan, Design of biodegradable, implantable devices towards clinical translation. *Nat. Rev. Mater.* **5**, 61–81 (2020).

73. H. Joo, Y. Lee, J. Kim, J.-S. Yoo, S. Yoo, S. Kim, A. K. Arya, S. Kim, S. H. Choi, N. Lu, H. S. Lee, S. Kim, S.-T. Lee, D.-H. Kim, Soft implantable drug delivery device integrated wirelessly with wearable devices to treat fatal seizures. *Sci. Adv.* **7**, eabd4639 (2021).

74. J. Koo, S. B. Kim, Y. S. Choi, Z. Xie, A. J. Bandodkar, J. Khalifeh, Y. Yan, H. Kim, M. K. Pezhouh, K. Doty, G. Lee, Y.-Y. Chen, S. M. Lee, D. D'Andrea, K. Jung, K. Lee, K. Li, S. Jo, H. Wang, J.-H. Kim, J. Kim, S.-G. Choi, W. J. Jang, Y. S. Oh, I. Park, S. S. Kwak, J.-H. Park, D. Hong, X. Feng, C.-H. Lee, A. Banks, C. Leal, H. M. Lee, Y. Huang, C. K. Franz, W. Z. Ray, M. MacEwan, S.-K. Kang, J. A. Rogers, Wirelessly controlled, bioresorbable drug delivery device with active valves that exploit electrochemically triggered crevice corrosion. *Sci. Adv.* **6**, eabb1093 (2020).

75. Y. Zhang, F. Liu, Y. Zhang, J. Wang, D. D'Andrea, J. B. Walters, S. Li, H.-J. Yoon, M. Wu, S. Li, Z. Hu, T. Wang, J. Choi, K. Bailey, E. Dempsey, K. Zhao, A. Lantsova, Y. Bouricha, I. Huang, H. Guo, X. Ni, Y. Wu, G. Lee, F. Jiang, Y. Huang, C. K. Franz, J. A. Rogers, Self-powered, light-controlled, bioresorbable platforms for programmed drug delivery. *Proc. Natl. Acad. Sci. U.S.A.* **120**, e2217734120 (2023).

76. S. Liu, Z. Jia, F. Yang, T. Ning, X. Gu, X. Niu, Y. Fan, Flexible transient bioelectronic system enables multifunctional active-controlled drug delivery. *Adv. Funct. Mater.* **33**, 2215034 (2023).

77. Y. T. Yi, J. Y. Sun, Y. W. Lu, Y. C. Liao, Programmable and on-demand drug release using electrical stimulation. *Biomicrofluidics* **9**, 022401 (2015).

78. M. Tokita, Time-lag method and transport properties of gel. *Jpn. J. Appl. Phys.* **34**, 2418–2422 (1995).

79. L. J. Cote, F. Kim, J. Huang, Langmuir−Blodgett assembly of graphite oxide single layers. *J. Am. Chem. Soc.* **131**, 1043–1049 (2008).

80. S. M. Won, J. Koo, K. E. Crawford, A. D. Mickle, Y. Xue, S. Min, L. A. McIlvried, Y. Yan, S. B. Kim, S. M. Lee, B. H. Kim, H. Jang, M. R. MacEwan, Y. Huang, R. W. Gereau IV, J. A. Rogers, Natural wax for transient electronics. *Adv. Funct. Mater.* **28**, 1801819 (2018).